Word count: 9117 (excluding abstract, figure captions, and references)

Revision 1

The effects of oxygen fugacity and sulfur on the pressure of vapor-saturation of magma

Ery C. Hughes[1,2,*], Philippa Liggins[3], Lee Saper[2,4], and Edward M. Stolper[2]

1 Te Pū Ao | GNS Science, National Isotope Centre/Avalon, Aotearoa New Zealand

2 Division of Geological and Planetary Science, Caltech, CA USA

3 Department of Earth Sciences, University of Cambridge, UK

4 School of Geosciences, University of Edinburgh, UK

*Correspondence (e.hughes@gns.cri.nz)

Abstract

Geobarometers are commonly used to determine the pressure (and hence depth) of magmatic bodies. For instance, at equilibrium, the concentration of dissolved volatiles in a vapor-saturated melt can be used as a barometer: this is the pressure of vapor-saturation (P^{v}_{sat}). Most determinations of P^{v}_{sat} assume that melt and vapor contain only oxidised C-O-H species. However, sulfur is the third most abundant volatile element in magmas and oxygen fugacity (f_{O2}) exerts a strong influence on the speciation of the melt and vapor. To explore how S and f_{O2} affect calculations of P^{v}_{sat}, we model a Hawaiian tholeiite that contains both reduced and oxidised C-O-H-S species in the melt and vapor. We find that excluding reduced C-O-H species in the system can result in significant underestimations of P^{v}_{sat} under reducing conditions ($\Delta FMQ < 0$). The

effect of S on P^{v}_{sat} is small except in the vicinity of the "sulfur solubility minimum" (SS^{min}; $0 < \Delta FMQ < +2$), where excluding S-bearing species can result in underestimates of P^{v}_{sat}.

The implications of these results depend on the volatile concentration of the system being investigated, its f_{O2}, and the melt composition and temperature. Our results suggest there will be little impact on P^{v}_{sat} calculated for mid-ocean ridge basalts because their f_{O2} is above where reduced C-O-H species become important in the melt and vapor, and yet below the SS^{min}. However, the f_{O2} of ocean island and arc basalts are close enough to the SS^{min} and their S concentrations high enough to influence P^{v}_{sat}. However, high CO_2 and H_2O concentrations are predicted to reduce the effect of the SS^{min}. Hence, P^{v}_{sat} calculated for shallowly trapped melt inclusions and matrix glass are more affected by the SS^{min} than deeply trapped melt inclusions. Lunar and martian magmas are typically more reduced than terrestrial magmas, and therefore accurate P^{v}_{sat} calculations for them require the inclusion of reduced C-O-H species.

Keywords: pressure of vapor saturation, thermodynamics, oxygen fugacity, carbon, hydrogen, sulfur

1 Introduction

The concentrations of dissolved volatiles (e.g., H_2O, CO_2) in the melt phase of magma are widely used to determine total pressure (P) (e.g., Anderson *et al.* 1989; Blundy and Cashman 2008). Such determinations are based on analyses of volatile components in quenched glasses coupled with the assumption that the melt from which the glass formed was in equilibrium with a

vapor prior to quenching. The basis of this approach is that for a given temperature (T) and assumed value of P, the partial pressure of each species in vapor (p_i) coexisting with melt can be calculated from the concentrations of volatile components dissolved in the melt. The pressure of vapor-saturation of the melt (P^v_{sat}) is then the unique P at which the sum of all the p_i's matches the total P.

This approach to determining P^v_{sat} for magmas has been widely applied to melt inclusions and matrix glasses, subject to several caveats (e.g., issues related to the fidelity with which glassy melt inclusions preserve the volatile concentrations present at the time of their entrapment: Anderson 1974; Roedder 1979; Anderson and Brown 1993; Portnyagin *et al.* 2008; Steele-Macinnis *et al.* 2011; Gaetani *et al.* 2012; Bucholz *et al.* 2013; Maclennan 2017; and the possibility of supersaturation of erupting melts with respect to vapor: Fine and Stolper 1986; Dixon *et al.* 1988; Jendrzejewski *et al.* 1997; Saal *et al.* 2002; Soule *et al.* 2012; Le Voyer *et al.* 2015, 2019; Aubaud 2022). For melt inclusions, this approach has led to many minimum estimates of the P (and therefore depth) of inclusion entrapment (e.g., Anderson Jr *et al.* 1989; Blundy and Cashman 2008), and such estimates have also has been used to "image" magmatic plumbing systems (e.g., Colman *et al.* 2015; Wanless *et al.* 2015; Camejo-Harry *et al.* 2018, 2019; Black and Andrews 2020; Wieser *et al.* 2021). When applied to sub-aqueously erupted matrix glass, it has been used to estimate eruption depths (e.g., Seaman *et al.* 2004; Coombs *et al.* 2006; Lund *et al.* 2018; Belgrano *et al.* 2021). This approach also returns the composition of the vapor phase in equilibrium with the melt at P^v_{sat}. This vapor composition can be used to understand whether the melt has undergone closed- or open-system degassing or has been buffered by a large volume of fluid (e.g., Spilliaert *et al.* 2006; Caricchi *et al.* 2018; Moretti *et al.* 2018). The vapor composition can also be used to reconstruct bulk melt inclusion compositions

at entrapment if a "shrinkage" vapor bubble has developed during cooling, provided that P^{v}_{sat} and the corresponding vapor composition are calculated at the closure T of bubble formation (e.g., Maclennan 2017; Tucker *et al.* 2019; Rasmussen *et al.* 2020).

Most efforts to calculate P^{v}_{sat} using this approach have assumed that the vapor contains only H_2O and CO_2 and the melt only contains H as hydroxyl ions (OH^-) and/or H_2O molecules (H_2O_{mol}), and C as carbonate ions (CO_3^{2-}) and/or CO_2 molecules ($CO_{2,mol}$) (e.g., VolatileCalc/MIMiC by Newman and Lowenstern, 2002; Rasmussen *et al.*, 2020; MagmaSat by Ghiorso and Gualda, 2015; VESIcal by Iacovino *et al.*, 2021; EVo by Liggins *et al.* 2020, 2022; Yip *et al.* 2022; MafiCH by Allison *et al.*, 2022; and various unnamed models such as those presented by Papale *et al.* 2006; Iacono-Marziano *et al.* 2012; and Duan 2014). These calculations do not generally consider the effects on P^{v}_{sat} and the corresponding vapor composition of the presence of reduced C-O-H (e.g., H_2, CO, CH_4) and S-bearing species in the vapor and melt. However, oxygen fugacity (f_{O2}) can play a significant role in the speciation and abundances of C-O-H-S volatile components in coexisting vapor and melt, and S is the third most abundant volatile element in most naturally occurring silicate magmas (e.g., Holloway and Blank 1994). Some studies have considered the importance of S and/or the effects of f_{O2} during degassing (e.g., Carroll and Webster 1994; Moretti and Papale 2004; Scaillet and Pichavant 2004; Kress *et al.* 2004; Gaillard *et al.* 2011; Burgisser *et al.* 2015; Wetzel *et al.* 2015; Lesne *et al.* 2015; Newcombe *et al.* 2017a; Liggins *et al.* 2020, 2022; Lo *et al.* 2021; Métrich 2021; Sun and Lee 2022; Wieser *et al.* 2022; Hughes *et al.* 2023). However, there has to our knowledge not yet been a systematic or quantitative investigation of these effects on calculations of P^{v}_{sat}.

We are particularly interested in the effects of the so-called "sulfur solubility minimum" (referred to here as the SS^{min} – see Hughes *et al.*, 2023) on calculated values of P^{v}_{sat} and vapor

composition. The SS^{min} corresponds to a minimum in the dissolved sulfur content of vapor-saturated melt with increasing f_{O2} at constant P and T in the f_{O2} range over which the speciation of S dissolved in the melt changes from S^{2-}- to S^{6+}-dominated. This phenomenon for melt + vapor equilibrium has been observed experimentally (e.g., Fincham and Richardson 1954; Katsura and Nagashima 1974; Carroll and Rutherford 1985; Backnaes and Deubener 2011; Lesne *et al.* 2015; Matjuschkin *et al.* 2016; Nash *et al.* 2019) and in various calculations (e.g., Fincham and Richardson 1954; Katsura and Nagashima 1974; Carroll and Rutherford 1985; Moretti *et al.* 2003; Moretti and Ottonello 2005; Backnaes and Deubener 2011; Baker and Moretti 2011; Lesne *et al.* 2015; Matjuschkin *et al.* 2016; Nash *et al.* 2019; Cicconi *et al.* 2020; Papale *et al.* 2022; Hughes *et al.* 2023). Hughes *et al.* (2023) used a simplified S-O system (i.e., without C-O-H species) to analyse the factors leading to the SS^{min}. They found the SS^{min} resulted in a maximum in P^{v}_{sat} with increasing f_{O2} at constant T and total S-content of the melt due to a maximum in p_{SO2} where the speciation of S in the melt changed from S^{2-}- to S^{6+}-dominated. If this f_{O2}-dependent maximum in P^{v}_{sat} extends to C-O-H-S-bearing systems, magma reservoir depths from melt inclusions and eruption pressures from matrix glasses based on calculations of P^{v}_{sat} that exclude S will be underestimated for magmas with f_{O2} values in the vicinity of the SS^{min}. Hence, it is important to understand quantitatively the behaviour of the SS^{min} in C-O-H-S systems most relevant to natural magmas.

In this paper, we extend the thermodynamic framework of Hughes *et al.* (2023) to include C-O-H-S vapor and melt species (Section 2), and we apply it to calculating P^{v}_{sat}. The model we use is most closely related to those of Gaillard *et al.* (2011, 2013), Baumgartner *et al.* (2017), Iacono-Marziano *et al.* (2017), Liggins *et al.* (2020, 2022), and Sun and Lee (2022). Our model is written in Python, can be run using Jupyter Notebook, and is available on github

This is the peer-reviewed, final accepted version for American Mineralogist, published by the Mineralogical Society of America.
The published version is subject to change. Cite as Authors (Year) Title. American Mineralogist, in press.
DOI: https://doi.org/10.2138/am-2022-8739. http://www.minsocam.org/

(https://github.com/eryhughes/Pvsat). Given this thermodynamic model, we explore predicted trends in P^{v}_{sat} with varying f_{O2} for a fixed volatile concentration in the melt (Section 3.1). We then explore: (1) how variations in the total amounts of H, C, and S dissolved in the melt influence the calculated value of P^{v}_{sat} (Section 3.2), especially the calculated effects of the predicted build-up of relatively insoluble C-O-H species at low f_{O2} (Section 3.2.1); and (2) the behavior of the SS^{min} in C- and H-bearing systems and the quantitative impact of this feature on calculated values on P^{v}_{sat} (Section 3.2.2). Finally, we apply the model to natural melt inclusions and matrix glasses from different tectonic settings on Earth, as well as lunar and martian magmas, to evaluate how calculated values of P^{v}_{sat} are influenced by these effects (Section 4).

2 Calculating the pressure of vapor-saturation and the vapor composition

Our goal is to calculate P^{v}_{sat}, the P at which a silicate melt of a fixed chemical composition (including the concentrations of dissolved volatile components in the melt) can coexist with vapor at a given T and f_{O2}. At this P, the sum of the p_i's of all species in the vapor (n different species, where each species is denoted with subscript i) in equilibrium with the melt equals the P of the system:

$$P = \sum_{i=1}^{n} p_i \,, \#(1)$$

and the mole fraction of each species in the vapor (x_i^v) is related to its p_i by:

$$p_i = \frac{f_i}{\gamma_i^v} = x_i^v P \,, \#(2)$$

This is the peer-reviewed, final accepted version for American Mineralogist, published by the Mineralogical Society of America.
The published version is subject to change. Cite as Authors (Year) Title. American Mineralogist, in press.
DOI: https://doi.org/10.2138/am-2022-8739. http://www.minsocam.org/

where f_i is the fugacity of species *i*, and γ_i^v is the fugacity coefficient of species *i* in the vapor (*v*). Determining P^v_{sat} requires finding the *P* that is equal to the sum of the p_i's of all molecular species in the vapor: i.e., solving equation (1). At a higher *P* than P^v_{sat}, the system is vapor-undersaturated. Hence, these calculations assume the melt is saturated with a vapor – if the melt is not vapor-saturated, the calculated *P* represents a minimum. At a lower *P* than P^v_{sat}, melt with the assumed concentrations of volatiles is supersaturated with respect to vapor and the melt is metastable (or potentially unstable if sufficiently supersaturated; e.g., Allabar and Nowak 2018; Sahagian and Carley 2020; Gardner *et al.* 2022). Given sufficient time, a vapor phase will exsolve from the supersaturated melt, reducing the volatile concentration of the melt such that equilibrium is achieved (i.e., such that equation (1) is satisfied at the fixed *P*, *T*, and bulk composition of the system). Calculating P^v_{sat} for a given melt composition requires choosing: (1) the species in the vapor that will contribute significantly to the total *P* and the homogenous vapor equilibria that relate them (Section 2.1); and (2) solubility functions that provide relationships between the melt composition and the p_i's (Section 2.2).

2.1 Species and homogeneous equilibria in the vapor

If H_2O and CO_2 are assumed to be the only vapor species, as is typical (see Section 1), equation (1) becomes:

$$P = \sum_{i=1}^{2} p_i = p_{H_2O} + p_{CO_2}. \#(3)$$

This is the peer-reviewed, final accepted version for American Mineralogist, published by the Mineralogical Society of America.
The published version is subject to change. Cite as Authors (Year) Title. American Mineralogist, in press.
DOI: https://doi.org/10.2138/am-2022-8739. http://www.minsocam.org/

147 A review of solubility models used to relate dissolved H_2O and CO_2 concentrations in the melt to
148 p_{H2O} and p_{CO2} is provided by Iacovino *et al.* (2021), which can be used to calculate P^{v}_{sat} via
149 equation (3). However, to investigate the effects of f_{O2} and S, we need to consider a C-O-H-S
150 vapor containing species in addition to those in equation (3). Although other species could be
151 added, we have considered the following vapor species: O_2, H_2, H_2O, CO, CO_2, S_2, SO_2, H_2S,
152 CH_4, and OCS, such that equation (1) becomes:

$$P = \sum_{i=1}^{10} p_i = p_{O_2} + p_{H_2} + p_{H_2O} + p_{CO} + p_{CO_2} + p_{S_2} + p_{SO_2} + p_{CH_4} + p_{H_2S} + p_{OCS}. \#(4)$$

153 The fugacities of these vapor species are related through the six linearly-independent
154 homogenous vapor equilibria given in Table 1. Details of our choice of equilibrium constants
155 and fugacity coefficients for vapor species are given in Supplementary Material Section 3.1.

156

157 **2.2 Solubility functions**

158 When melt and vapor are in equilibrium, there is a function (the "solubility function") that
159 relates the dissolved concentration in the melt of a volatile component to the partial pressure(s)
160 of one (or more) species in the vapor. We use known or likely solubility mechanisms (i.e.,
161 chemical reactions between vapor and melt) to constrain the functional forms of the various
162 solubility functions (e.g., Fincham and Richardson 1954; Stolper 1982a; Silver and Stolper 1985;
163 Dixon and Stolper 1995; Gaillard *et al.* 2011, 2013; Liggins *et al.* 2020, 2022; Thomas and
164 Wood 2021; Hughes *et al.* 2023). The key point is that an accurate solubility function allows

calculation of the fugacities of certain vapor species given volatile concentrations in coexisting melt, from which their p_i's can be calculated using equation (2).

Based on our chosen vapor species (Section 2.1) and the assumption of a basaltic melt, we consider the following dissolved C-O-H species in the melt: molecular H_2 ($H_{2,mol}$; e.g., Gaillard *et al.* 2003; Kadik *et al.* 2004; Mysen *et al.* 2011; Hirschmann *et al.* 2012), hydroxyl ions (OH^-; e.g., Burnham and Davis 1974; Mysen *et al.* 1980; Stolper 1982a), molecular H_2O (H_2O_{mol}; e.g., Stolper 1982a; Dixon and Stolper 1995; Lesne *et al.* 2011), molecular CO (CO_{mol}; e.g., Brooker *et al.* 1999; Armstrong *et al.* 2015; Yoshioka *et al.* 2019), carbonate ions (CO_3^{2-}; e.g., Stolper and Holloway 1988; Blank and Brooker 1994; Dixon *et al.* 1995), and molecular CH_4 ($CH_{4,mol}$; e.g., Ardia *et al.* 2013; Mysen 2013). For dissolved S, we assume sulfide ions ($*S^{2-}$, where * refers to sulfide complexes in the melt other than H_2S), sulfate ions (SO_4^{2-}), and molecular H_2S (H_2S_{mol}) are the dominant S-bearing species in the melt (e.g., Fincham and Richardson 1954; Paris *et al.* 2001; O'Neill and Mavrogenes 2002, 2022; Clemente *et al.* 2004; Métrich *et al.* 2009; Wilke *et al.* 2011; Klimm *et al.* 2012; Lesne *et al.* 2015; O'Neill 2021; Boulliung and Wood 2022). Although other S-bearing species have been observed spectroscopically, they are not thought to be significant in natural Fe-bearing melts (e.g., Métrich *et al.* 2009; Wilke *et al.* 2011). For each dissolved species in the melt, the corresponding solubility mechanism (heterogeneous melt-vapor equilibrium) is given in Table 2.

The solubility of a particular volatile species can depend on *P*, *T*, melt composition, and the presence of other volatile species. To illustrate our approach and the trends that it predicts, we have chosen solubility functions appropriate for a Hawaiian tholeiite (detailed in Table 2). However, other solubility functions can be incorporated into our framework (see Supplementary Material Section 3.2 for details) and we emphasize that tailored solubility functions for specific

melt compositions are required if the goal is detailed petrologic interpretations of particular samples. For $H_{2,mol}$, we use the solubility function of Hirschmann *et al.* (2012) for basalt but modify it to relate $H_{2,mol}$ in ppm to f_{H2} in bar (equation (11) in Table 2; see Supplementary Material Section 3.2.3 for details). For the solubility of H_2O, we use the approximation of Sievert's law; i.e., that f_{H2O} is proportional to the square of the mole fraction or concentration of the total H dissolved as oxidised species (i.e., combination of OH^- and H_2O_{mol}, expressed as H_2O: H_2O_T; see equation (12) in Table 2); this has been shown to be a good approximation up to $\lesssim$6.4 wt% H_2O (e.g., Burnham 1979; Stolper 1982b; Ghiorso and Gualda 2015). We use the data compilation of Allison *et al.* (2019) to calibrate this solubility function for basaltic melts (see Supplementary Material Section 3.2.2 for details). For CO_{mol}, we reparameterise the solubility function of Armstrong *et al.* (2015) (equation (13) in Table 2) using data from Wetzel *et al.* (2013), Stanley *et al.* (2014), and Armstrong *et al.* (2015) (see Supplementary Material Section 3.2.3 for details). The solubility of CO_3^{2-} is highly dependent on melt composition (e.g., Spera and Bergman 1980; Blank and Brooker 1994; Holloway and Blank 1994; Shishkina *et al.* 2014; Allison *et al.* 2019). We use the solubility function of Dixon *et al.* (1995) (equation (14) in Table 2), which is based on data for Hawaiian tholeiites and MOR basalts, although this can be modified for other basaltic compositions (e.g., data from Allison *et al.* (2019); see Supplementary Material Section 3.2.1 for details). For $CH_{4,mol}$, we use the solubility function of Ardia *et al.* (2013) (equation (15) in Table 2). We use O'Neill (2021) for the $*S^{2-}$ solubility function and O'Neill and Mavrogenes (2022) for SO_4^{2-} (equation (16) and (17), respectively, in Table 2). We reparameterise a solubility function for H_2S_{mol} from Clemente *et al.* (2004) and Lesne *et al.* (2015) (equation (18) in Table 2) using basaltic data from Moune *et al.* (2009) and Lesne *et al.* (2015) (see Supplementary Material Section 3.2.5 for details). We include H_2S_{mol} as

a separate species because it is simpler to ensure (compared to its inclusion as another $*S^{2-}$ species; see, O'Neill 2021) that H mass balance is satisfied (i.e., H in the melt is partitioned between H_2O, H_2S, H_2, and CH_4 species) and thus that we do not overestimate the S content of the melt.

In addition to the solubility functions, our thermodynamic model includes homogeneous equilibrium between Fe^{2+} (FeO) and Fe^{3+} ($FeO_{1.5}$) in the melt, where melt Fe^{3+}/Fe^{2+} is related to f_{O_2}, melt composition, P, and T (we use Kress and Carmichael 1991, but other parameterisations can be used). Finally, we check if the melt is supersaturated with respect to sulfide melt, anhydrite, or graphite; if so, the calculations we present are metastable relative to precipitation of one or more of these phases and we state this whenever it is the case. The melt is supersaturated with respect to sulfide melt if the $*S^{2-}$ content of the melt is greater than the sulfide content at sulfide saturation (S^{2-}CSS, assuming the sulfide is pure FeS; O'Neill 2021); with respect to anhydrite if the SO_4^{2-} content of the melt is greater than the sulfate content at anhydrite saturation (S^{6+}CAS, Zajacz and Tsay 2019); and with respect to graphite if f_{CO2}/f_{O2} is greater than the equilibrium constant for $C_{graphite} + O_2 = CO_2$ (Holloway *et al.* 1992) (other parameterisations for saturation of additional phases can be included in our model).

2.3 Deriving melt speciation to calculate fugacities and partial pressures

Given P, T, and f_{O2}, the fugacities of most species in the coexisting vapor can be calculated from concentrations of dissolved volatile species in the melt via equations (11–18) in Table 2. The homogeneous equilibria in the vapor phase described by equations (7) and (10) in Table 1 can then be used to calculate fugacities of the assumed insoluble species SO_2 and OCS,

233 respectively. These fugacities can be converted to partial pressures using equation (2) and
234 summed together to calculate P^{v}_{sat} as in equation (4). However, typically only the *bulk*
235 concentrations of H, C, and S dissolved in the melt are known, not the concentration of
236 individual H, C, and S-bearing *species*. For instance, some analytical techniques used to measure
237 volatile concentrations (e.g., secondary ion mass spectrometry) provide no information on the
238 identity or concentrations of different melt species. However, even if an analytical technique can
239 quantify the concentrations of some species (e.g., Fourier transform infrared spectroscopy for
240 H_2O_{mol} vs. OH^- or $CO_{2,mol}$ vs. CO_3^{2-}), other dissolved species (e.g., H_2, CO, CH_4) are typically
241 not quantifiable at natural abundances. Moreover, the measured speciation could have changed
242 on quenching to a glass (e.g., Stolper 1989; Dingwell and Webb 1990; Morizet *et al.* 2001;
243 Behrens and Nowak 2010; Konschak and Keppler 2014; Nash *et al.* 2019).

244 To deal with this, we solve for the speciation of the melt, subject to the constraints of: the
245 heterogeneous melt-vapor equilibria in Table 2; homogeneous vapor equilibria in Table 1; mass
246 balance given the specified bulk concentrations of H, C, and S in the melt; and the intensive
247 parameters T, f_{O2}, and P. In this way, the total H, C, and S concentrations measured in the glass
248 are distributed into equilibrium concentrations of the various dissolved species. This is done
249 iteratively, assuming an initial value of P (details of the choice of P are given in the next
250 section). Firstly, all H is assumed to be H_2O_T, all C is CO_3^{2-}, and all S is $*S^{2-}$. Then the
251 concentrations of the other melt species ($H_{2,mol}$, CO_{mol}, $CH_{4,mol}$, H_2S_{mol}, and SO_4^{2-}) are calculated
252 at the given f_{O2}, T, and P using the equations in Tables 1 and 2. The total amounts of H, C, and S
253 in the melt is then calculated by summing the amounts of these elements in all the melt species.
254 The calculated totals will be higher than the known bulk composition of the melt: e.g., for H, all
255 H dissolved in the melt was initially assumed to be H_2O_T, but after the first iteration, there is

This is the peer-reviewed, final accepted version for American Mineralogist, published by the Mineralogical Society of America.
The published version is subject to change. Cite as Authors (Year) Title. American Mineralogist, in press.
DOI: https://doi.org/10.2138/am-2022-8739. http://www.minsocam.org/

additional H in the melt in form of $H_{2,mol}$, $CH_{4,mol}$, and H_2S_{mol}. Based on the difference between these, new values for the concentrations of H_2O_T, CO_3^{2-}, and $*S^{2-}$ are estimated, and the process is repeated until H, C, and S satisfies mass balance within a defined limit. Note that oxygen is not mass balanced as f_{O2} is an independent variable in these calculations and different choices of f_{O2} lead to different bulk oxygen contents of the melt. Further details are provided in Supplementary Material Section 4.

These calculations require f_{O2} as an input. When trying to determine P^v_{sat} for a natural sample, this could be constrained from measurements of Fe^{3+}/Fe_T or S^{6+}/S_T in the glass (e.g., Carroll and Rutherford 1988; Kress and Carmichael 1991; although changes may occur on the quench: Nash *et al.* 2019) or by independent oxybarometry. Here, we have chosen f_{O2} as an independent variable to evaluate the effects of variation in f_{O2} on P^v_{sat} at constant total dissolved volatile contents. Details are given in Supplementary Material Section 3.2.6 for how f_{O2} is chosen and the reference buffers we use in reporting f_{O2}.

2.4 Solving for P^v_{sat} and vapor composition

It is important to note that γ_i^v, C_i, and f_{O2} all depend on the P chosen for the calculations described in Section 2.3. Therefore, P^v_{sat} must also be calculated iteratively. The initial guess for P (P_0) is chosen to be high (e.g., 40,000 bars). The speciation of the melt is iteratively solved at the given f_{O2}, T, P_n, and bulk volatile content of the melt (H, C, and S) as described in Section 2.3. This gives the concentration of specific dissolved species in the melt; f_i (including insoluble vapor species); p_i using equation (2); and P^v_{sat} using equation (4). The next guess for P (P_1) is set as the sum of the partial pressures given by the previous guess for P (i.e., $P^v_{sat}[P_0]$) and then the

iteration is repeated. After each iteration, the difference between P_n and P^v_{sat} is evaluated: dP = $P_n - P^v_{sat}[P_n]$. If dP after the iteration is less than the specified tolerance (here we use 0.1 bar), P^v_{sat} is taken to have been found. If dP is greater than the specified tolerance, $P_{n+1} = P^v_{sat}[P_n]$ and the calculations of melt speciation and P^v_{sat} are repeated until dP is less than the specified tolerance. Once the calculation has converged, the concentration of all species in the melt and vapor are calculated at P^v_{sat}.

3 Effects of f_{O2} and H, C, and S concentrations on vapor-saturation pressures and vapor compositions

To isolate and analyze the effects of f_{O2} and H, C, and S concentrations on P^v_{sat} and on the composition of the saturating vapor, we use the same base melt composition and T for all calculations in this section. The melt composition is the Hawaiian tholeiite used in Hughes *et al.* (2023) at T = 1200 °C.

3.1 P^v_{sat} for a reference case with fixed total volatile concentrations in the melt

In this section, we describe the calculated P^v_{sat} with varying f_{O2} for a melt containing fixed total dissolved C and H contents (Figure 1). The total concentration of C is 273 ppm (all ppm are by weight, corresponding to 1000 ppm of CO_2 if all C were dissolved as CO_2: we refer to this CO_2 equivalent concentration as CO_2-eq) and H is 3357 ppm (corresponding to 3 wt% H_2O-eq). In case 1, all C-O-H species in the melt and vapor are oxidized. Hence, H_2O and CO_2 are assumed to be the only vapor species and H_2O_T (i.e., the combination of both OH^- and H_2O_{mol}) and CO_3^{2-} are the only volatile-bearing melt species (Section 3.1.1). This is equivalent to most P^v_{sat}-calculators currently in use (e.g., Newman and Lowenstern 2002; Papale *et al.* 2006;

Iacono-Marziano *et al.* 2012; Duan 2014; Ghiorso and Gualda 2015; Iacovino *et al.* 2021; Allison *et al.* 2022). In case 2, both oxidized and reduced C-O-H species are present in the melt and vapor phase (Section 3.1.2). Lastly, we add a fixed amount of S to case 2 (1000 ppm S-eq), leading to case 3 where S-bearing species are present in addition to the C-O-H species included in case 2 (Section 3.1.3). Two additional cases are described in Supplementary Material Section 6.3: case 2', which is the same as case 2 except reduced C-O-H species are assumed to be completely insoluble in the melt; and case 3', which is the same as case 3 except H_2S_{mol} is treated as insoluble in the melt.

3.1.1 Case 1: only oxidised C-O-H species in the melt and vapor.

This case will be used as a reference for comparison to the other cases that we consider. For this case, P^v_{sat}, p_i's (p_{CO2} and p_{H2O}), melt speciation, and vapor composition (x^v_{H2O} and x^v_{CO2}) are independent of f_{O2} (black lines in Figure 1 and Figure 2). If the solubility functions for CO_3^{2-} and H_2O_T were dependent on the Fe^{3+}/Fe_T of the melt, P^v_{sat}, p_i's, and vapor composition would depend on f_{O2}. However, melt speciation would still be independent of f_{O2} because of the assumption that there are no other dissolved C-O-H species. Wieser *et al.* (2022) found that available models (e.g., Papale *et al.* 2006; Shishkina *et al.* 2014; Ghiorso and Gualda 2015) suggest H_2O solubility is relatively insensitive to Fe^{3+}/Fe_T (also observed by Newcombe *et al.*, 2017), whereas CO_2 solubility is sensitive to Fe^{3+}/Fe_T. However, they found the effects are highly uncertain due to a lack of experimental data to calibrate the Fe^{3+}/Fe_T dependence of H_2O and CO_2 solubility. We show a comparison to VolatileCalc in Figure 1 (and other models in

Supplementary Material Section 5, Figures S7 sand S8), which highlights how much different solubility functions (especially for CO_2) can affect calculations of P^v_{sat}.

3.1.2 Case 2: oxidised and reduced C-O-H species in the melt and vapor.

For case 2, decreasing f_{O2} results in the fractions of the total H and C dissolved in the melt as reduced species increasing and as oxidised species decreasing (Figure 2c), which is reflected in the corresponding p_i's and x^v_i's (Figure 2a and e). H and C behave differently at $\Delta FMQ < -1$, with a large decrease in p_{CO2} but very little change in p_{H2O}. This is because the equilibrium constants for homogeneous equilibria (5) and (6) in Table 1 result in p_{CO} beginning to increase significantly with decreasing f_{O2} (from ~0 to ~1200 bars from $\Delta FMQ=0$ to -3) at a higher f_{O2} than that at which p_{H2} begins to increase. Hence, the amount of CO_3^{2-} in the melt decreases substantially over the f_{O2} range covered in the figure, whereas there is less change in the amount of H_2O_T (i.e., compare the solid blue and red curves in Figure 2c).

For $\Delta FMQ \gtrapprox 0$, P^v_{sat} is approximately equal to that assuming the vapor only contains CO_2 and H_2O (Figure 1) because the p_i's and x^v_i's of H_2, CO, and CH_4 are negligible in the vapor (red and blue curves in Figure 2a and e). With decreasing f_{O2} below $\Delta FMQ \approx 0$, the p_i's of these reduced vapor species increase, while those of H_2O and CO_2 decrease, but the increases for the reduced species are larger (Figure 2a). Hence, there is a significant increase in P^v_{sat} with decreasing f_{O2} when the reduced C-O-H species are included (Figure 1). This is due to the build-up of reduced C-O-H species in the system that are less soluble than oxidised C-O-H species (e.g., Scaillet and Pichavant 2004; Wetzel *et al.* 2015; Newcombe *et al.* 2017a). If the reduced C-O-H species are assumed to be completely insoluble in the melt, the increase in P^v_{sat} is even

342 greater (see Supplementary Material Section 6.3.1). For the conditions shown in Figure 2,
343 graphite is not stable.

344 **3.1.3 Case 3: S-bearing species in the melt and vapor.**

345 The variations with f_{O2} for the C- and H-bearing vapor and melt species for the S-bearing
346 case 3 are similar to those for the S-free case 2 (i.e., compare the blue and red curves Figure 2).
347 This reflects: (1) the relatively low concentration of S in the melt (i.e., H_2O-eq = 3 wt% vs. S-eq
348 = 0.1 wt%); and (2) the relatively high solubility of S in the melt compared to CO_2 such that the
349 vapor has a high C/S ratio relative to the melt. Hence, the p_i's of S-bearing species are small and
350 a small fraction of P^v_{sat} under all conditions shown in Figure 2b. Another factor is the assumed
351 insolubility of OCS species in the melt for this case, which means dissolved S has a negligible
352 effect on the concentrations of C-bearing species in the melt. For the conditions shown in Figure
353 2, graphite, sulfide, and anhydrite are not stable.

354 Sulfur is dissolved in the melt nearly entirely as S^{2-} at low f_{O2} (ΔFMQ $\lesssim$ 0) and SO_4^{2-} at high
355 f_{O2} (ΔFMQ $\gtrsim$ 2) (Figure 2d; e.g., Fincham and Richardson 1954; Moretti and Ottonello 2005,
356 2003; Moretti and Papale 2004; Gaillard and Scaillet 2009, 2014; Baker and Moretti 2011;
357 Gaillard *et al.* 2011, 2013, 2015; Baumgartner *et al.* 2017; Moretti 2021). Additionally, at low
358 f_{O2} (ΔFMQ $\lesssim$ 0), H_2S_{mol} and $*S^{2-}$ are present in roughly equal molar concentrations in the melt
359 (Figure 2d). By combining equations (9), (16), and (18) in Table 1 and Table 2, we obtain the
360 following expression for the ratio of S^{2-} dissolved in the melt as H_2S_{mol} to that dissolved as $*S^{2-}$:

361 $$\frac{x^m_{H_2S_{mol}}}{x^m_{*S^{2-}}} = \frac{K_{HS} C_{H_2S_{mol}}}{C_{*S^{2-}}} f_{H_2O}. \quad (20)$$

This is the peer-reviewed, final accepted version for American Mineralogist, published by the Mineralogical Society of America.
The published version is subject to change. Cite as Authors (Year) Title. American Mineralogist, in press.
DOI: https://doi.org/10.2138/am-2022-8739. http://www.minsocam.org/

Therefore, $H_2S_{mol}/{}^*S^{2-}$ increases linearly with increasing f_{H2O} (or equivalently with $(x^m_{H_2O_T})^2$ based on equation 12) if the melt composition is otherwise fixed (i.e., at given f_{H2O}, P, and T, the $H_2S_{mol}/{}^*S^{2-}$ ratio depends only on the ratio of the solubilities in equation 19). The ratio is independent of f_{S2} and f_{O2} (except through the dependence of f_{H2O} on f_{O2} and f_{H2} through reaction 5). The relationship between S^{6+}/S^{2-}_T and f_{O2} (where S^{2-}_T is the total S dissolved as sulphide, given by ${}^*S^{2-} + H_2S$) can be derived by combining equations (17) (Table 2) and (20):

$$\frac{x^m_{SO_4^{2-}}}{x^m_{S_T^{2-}}} = \frac{x^m_{SO_4^{2-}}}{x^m_{H_2S_{mol}} + x^m_{*S^{2-}}} = \frac{C_{SO_4^{2-}}}{C_{H_2S_{mol}} K_{SH} f_{H_2O} + C_{*S^{2-}}} \left(f_{O_2}\right)^2 \approx \left[\frac{C_{SO_4^{2-}}}{K_{HS} C_{H_2S} \frac{(x^m_{H_2O_T})^2}{C_{H_2O_T}} + C_{*S^{2-}}}\right] \left(f_{O_2}\right)^2. \quad (21)$$

Hence, SO_4^{2-}/S^{2-}_T depends on $(f_{O2})^2$, as is the case for $SO_4^{2-}/{}^*S^{2-}$ (e.g., Wallace and Carmichael 1994; Matthews *et al.* 1999; Moretti and Ottonello 2005; Métrich *et al.* 2009; Jugo *et al.* 2010; Moretti 2021; Hughes *et al.* 2023), but with different slopes.

At all values of f_{O2} covered by our modeling, p_{S2} contributes negligibly to the sum of the p_i's of the S-bearing species (Figure 3). At f_{O2} lower than ΔFMQ $\sim$ +0.4, H_2S is predicted to become the dominant S-bearing vapor species, followed by OCS (Figure 3). The decreases in p_{H2S} and p_{OCS} with increasing f_{O2} seen in Figure 3 between +0.40 $\lesssim$ ΔFMQ $\lesssim$ +1.5 results from the proportionality of both f_{H2S} (equation 9; Table 1) and f_{OCS} (equations 6, 7, and 9; Table 1) to $(f_{O2})^{-0.5}$. As p_{H2S} and p_{OCS} decrease, p_{SO2} increases with increasing f_{O2}, with p_{SO2} surpassing p_{H2S} at ~ΔFMQ+0.4 (Figure 3). For this melt composition, there is a maximum in p_{SO2} at ΔFMQ+1.28, where both S^{2-}_T and SO_4^{2-} species are dissolved in the melt in subequal amounts (Figure 3; there is also a much smaller maximum in p_{S2} at ΔFMQ+0.77). When S^{2-}_T is the dominant form of S dissolved in the melt, p_{S2} and p_{SO2} are respectively proportional to $(f_{O2})^1$ and

382 $(f_{O2})^{1.5}$ (equations 6, 7, and 16 in Tables 1 and 2). In contrast, when SO_4^{2-} dominates, p_{S2} and p_{SO2}
383 are respectively proportional to $(f_{O2})^{-3}$ and $(f_{O2})^{-0.5}$ (equations 6, 7, and 17 in Table 2) . As
384 discussed in Hughes et al. (2023), this change in the sign of the dependence of the derivative of
385 p_{SO2} and p_{S2} with respect to f_{O2} results in a maximum in p_{SO2} and p_{S2} in a C- and H-free system.
386 The same effect produces the maximum in P^v_{sat} at ΔFMQ+1.19 demonstrating the SS^{min} is a
387 general feature of S-bearing basaltic magmas at relatively oxidising conditions (Figure 3)

388 Even though S-bearing species are minor components of the vapor ($x^v_i < 0.03$, where $i = S_2$,
389 SO_2, H_2S, OCS; Figure 2f), their presence in case 3 influences P^v_{sat}. At all the f_{O2} values shown,
390 P^v_{sat} for case 3 is greater than case 2 (compare the yellow and blue curves in Figure 1). At low f_{O2}
391 (ΔFMQ < 0), this is due to the addition of H_2S and OCS to the vapor for case 3 (by up to ~20
392 bars at ΔFMQ = 0), which are not present in case 2. Additionally, the changing behaviour of S-
393 bearing species in the melt and vapor with f_{O2} (mainly H_2S and SO_2) results in the SS^{min} seen in
394 Figure 1. The overall behaviour of case 3 shown in Figure 3 is similar to that calculated for the
395 S-O (i.e., H- and C-absent, referred to as case 4) system presented in Hughes *et al.* (2023).
396 However, the magnitude and f_{O2}-position of the maximum in P^v_{sat} are different, reflecting the
397 influence of C and H on the system (more details in Supplementary Material Section 6.2).

398 Lesne *et al.* (2015) calculated $p_{H2S} + p_{SO2}$ for vapor coexisting with a basaltic melt in a C-free
399 system (i.e., the vapor was assumed to contain only S-O-H species) for varying f_{O2} at constant
400 dissolved S-eq, dissolved H_2O-eq, *T*, and *P*. They predicted that ignoring S-bearing vapor
401 species could lead to underestimates of P^v_{sat} of 10^2–10^3 bars at ~2000 bars. However, in contrast
402 to our results, their model produced a local *minimum* in P^v_{sat}, stating: "*It is only within the*
403 *minimum of sulfur solubility, i.e. around NNO ± 0.5* [~ΔFMQ+0.2 to +1.2]*, that ignoring partial*

pressure of S-bearing species does not greatly affect gas saturation calculations". The behaviour predicted by Lesne *et al.* (2015) assumes that the only S-bearing species in the melt are H_2S_{mol} and $SO_{2,mol}$. However, there is evidence for other dissolved S^{2-} species under reducing conditions in addition to H_2S_{mol} in natural silicate melt compositions (e.g., FeS, CaS; O'Neill 2021). Additionally there is no evidence for $SO_{2,mol}$ in natural silicate melt compositions under oxidising conditions, whereas SO_4^{2-} has been observed spectroscopically (e.g., Wilke *et al.* 2011). Therefore, we infer that SS^{min} will result in a local maximum in P^v_{sat} for silicate melts in nature, rather than a local minimum. However, if there are systems where the dominant oxidised S-bearing species in the melt is $SO_{2,mol}$ and H_2S_{mol} dominates over other dissolved sulfide species at reduced conditions, a minimum in P^v_{sat} might occur.

3.2 Varying the concentration of volatiles

We now investigate how variations in the concentrations of volatiles (i.e., bulk concentrations of C, H, and S in the melt) affect the relationship between P^v_{sat} and f_{O2}. This calculation uses the full C-O-H-S system with the same melt and vapor species as in case 3, but we allow the dissolved total volatile contents to vary between 0–5 wt% H_2O-eq, 0–2000 ppm CO_2-eq, and 0–2000 ppm S-eq.

We first calculate P^v_{sat} for a fully-oxidised, S-free reference system comparable to case 1 between 0–5 wt% H_2O-eq and 0–2000 ppm CO_2-eq, shown as isobars in Figure 4a. The differences between this reference case and the full C-O-H-S system are contoured in Figure 4b–d, where the contours are for constant values of $\Delta P^v_{sat} = P^v_{sat}$[C-O-H-S] – P^v_{sat}[oxidised C-O-H reference state]. Case 3 (3 wt% H_2O-eq, 1000 ppm CO_2-eq, and 1000 ppm S-eq) described in

This is the peer-reviewed, final accepted version for American Mineralogist, published by the Mineralogical Society of America.
The published version is subject to change. Cite as Authors (Year) Title. American Mineralogist, in press.
DOI: https://doi.org/10.2138/am-2022-8739. http://www.minsocam.org/

Section 3.1.3 is shown by the dashed grey horizontal lines in Figure 4b–d. Figure 4b has variable S (0–2000 ppm S-eq) at constant H (3 wt% H_2O-eq) and C (1000 ppm CO_2-eq); Figure 4c has variable H (0–5 wt% H_2O-eq) at constant S (1000 ppm S-eq) and C (1000 ppm CO_2-eq); and Figure 4d has variable C (0–2000 ppm CO_2-eq) at constant H (3 wt% H_2O-eq) and S (1000 ppm S-eq). In the following two subsections, we emphasize two features of Figure 4: (1) The increase in P^{v}_{sat} with decreasing f_{O2} at low f_{O2} ($\Delta FMQ \lesssim 0$) due to the build-up of relatively insoluble reduced C-O-H species in the vapor (Section 3.2.1); and (2) the local maximum in P^{v}_{sat} at intermediate f_{O2} ($\Delta FMQ \approx +0.5$ to $+1.5$ for this melt composition), which is a manifestation of the SS^{min} (Section 3.2.2).

3.2.1 Build-up of relatively insoluble reduced C-O-H species in the vapor.

At any given y-value on Figure 4b–d (i.e., a horizontal slice), ΔP^{v}_{sat} increases with decreasing f_{O2} for $\Delta FMQ \lesssim 0$. This is due to the build-up of reduced C-O-H species in the vapor because these species are less soluble in the melt than their oxidised counterpart species (e.g., Scaillet and Pichavant 2004; Wetzel *et al.* 2015; Newcombe *et al.* 2017a; discussed in Section 3.1.2). The contours of ΔP^{v}_{sat} also get closer together with decreasing $\log_{10}(f_{O2})$, reflecting the concave up shapes of the curves shown in Figure 1. However, the magnitude of the predicted effects – and even their signs – could be changed if future experiments were to demonstrate significantly lower or higher solubilities of these reduced species.

Contours of ΔP^{v}_{sat} with constant H and C contents but variable S contents are near-vertical; i.e., variations in the S content of the melt have only small effects on ΔP^{v}_{sat} (Figure 4b). This is because S-bearing species represent such small proportions of the vapor at low f_{O2} (e.g., <30 bars

448 with 1000 ppm S-eq for ΔFMQ $\lesssim$ 0; black solid curve in Figure 3). Although the S content of the
449 melt is changing along each contour in Figure 4b, neither the direct impact of these changes
450 through variations of the p_i's of S-bearing species nor their indirect effects on the p_i's of the C-O-
451 H species result in significant effects on P^v_{sat}.

452 Contours of ΔP^v_{sat} with constant S and C contents but variable H contents are also near-
453 vertical (Figure 4c), whereas for constant H and S but variable C they are steeply, positively
454 sloped and concave up (Figure 4d). Therefore, increasing the C content of the melt has a greater
455 effect on increasing ΔP^v_{sat} with decreasing f_{O2} than increasing the H content of the melt, even
456 though the absolute concentration of C is far smaller. This reflects the increase in the relatively
457 insoluble CO-species in the vapor with decreasing f_{O2} by conversion from CO_2 to CO (reaction
458 6) occurs at a higher f_{O2} than the increase in the H_2 species by conversion from H_2O with
459 decreasing f_{O2} (reaction 5) (see Section 3.1.2).

460 Graphite and anhydrite are not stable under the conditions shown in Figure 4. However,
461 sulfide is stable above the white dotted curves in Figure 4b and c (but nowhere in Figure 4d
462 because the S and H content of the melt are too low) and hence the calculations are metastable in
463 this region (see Hughes et al., 2023, for explanations of the shape of the sulfide-stable curve).
464 This shows that sulfide is stabilised at low f_{O2} (ΔFMQ < 0), high dissolved S (>1000 ppm S), and
465 high dissolved H_2O (>3.5 wt% H_2O-eq because of the effect of dilution on S^{2-}CSS).

466

This is the peer-reviewed, final accepted version for American Mineralogist, published by the Mineralogical Society of America.
The published version is subject to change. Cite as Authors (Year) Title. American Mineralogist, in press.
DOI: https://doi.org/10.2138/am-2022-8739. http://www.minsocam.org/

3.2.2 The sulfur solubility minimum in C- and H-bearing melts.

A near-vertical "ridge" defining a maximum in ΔP^{v}_{sat} at +0.5 < ΔFMQ < +1.5 is visible in Figure 4b–d. The trace of this ridge with varying volatile contents is shown in each panel as a black curve. For ease of comparison, these three traces are superimposed in Figure 5b where volatile concentrations along the "ridge" are plotted vs. the f_{O2}-position of the ridge. Figure 5a also superimposes these three traces of the ridge, in this case plotting volatile concentration vs. ΔP^{v}_{sat}, the height of the ridge.

The ΔP^{v}_{sat} maximum in Figure 4b–d is the signature of the SS^{min}, and it is also closely associated with maxima in the sum of the p_i's of S-bearing vapor species (especially p_{SO2}; Figure 3; and Hughes et al., 2023). Hence, the ridge in calculated ΔP^{v}_{sat} disappears in the S-free systems (i.e., near the x-axis in Figure 4b) and increases in height with increasing total dissolved S in the melt coexisting with vapor (e.g., with increasing S in Figure 4b). The interactions among C-, H-, and S-bearing species in the melt and vapor result in the systems described here being more complex than the simple cases considered by Hughes *et al.* (2023) (Sections 3.1.3). Nevertheless, our modeling predicts that this feature persists robustly in basaltic systems saturated with C-O-H-S vapor.

The f_{O2} value of the maximum in ΔP^{v}_{sat} varies little (+0.97 < ΔFMQ < +1.38) over the ranges in S-eq, H_2O-eq, and CO_2-eq explored here (Figure 5b). In contrast, the height of the ΔP^{v}_{sat} maximum does depend on the volatile contents of the melt (Figure 5a). The maximum in ΔP^{v}_{sat} reflects competing reactions involving dissolved S (Section 3.1.3; e.g., Hughes *et al.,* 2023). Hence, its magnitude increases with increasing S-eq because p_{SO2} is proportional to the total sulfur content of the melt (yellow line in Figure 5a; derivation in Supplementary Material

Section 6.1). However, $\Delta P^{v}_{sat} \neq 0$ at S-eq = 0 ppm, reflecting the presence of small but non-negligible quantities of reduced C-O-H species in the vapor such that $\Delta P^{v}_{sat} > 0$. The build-up of relatively insoluble C-O-H species (especially CO) contributes sufficiently to the ΔP^{v}_{sat} value that it begins to interfere with and obscure the SS^{min} at low S such that the maximum in ΔP^{v}_{sat} disappears before S_T reaches zero (e.g., yellow curves in Figure 5 terminate at $S_T > 0$). Increasing CO_2-eq in the melt causes the magnitude of the ΔP^{v}_{sat} maximum to decrease. The magnitude of the ΔP^{v}_{sat} maximum first increases then decreases with increasing H_2O-eq, highlighting the complex interplay between H-, C-, and S-bearing melt and vapor species.

4 Implications

Figure 4 emphasizes that calculations of the magnitude and exact position of the SS^{min} and their impact on calculations of P^{v}_{sat} will depend on precise knowledge of the volatile solubility functions, through which the complex interplay discussed in Section 3 must ultimately be modeled. Complete and accurate parameterizations of the solubilities in Table 2 in terms of the major element composition of the melt, f_{O2}, and the concentrations of each volatile component are needed for accurate calculations of P^{v}_{sat}. It is important to be aware of these uncertainties to avoid over-interpretation of the calculated absolute values of P^{v}_{sat}. For example, uncertainty in the parameters used in the model (e.g., solubilities and their parameterization, vapor fugacity coefficients) and analytical errors on the melt composition (major, minor, and volatile species, as well as iron oxidation state) can result in significant uncertainties in the accuracy of calculated values of P^{v}_{sat} (see Supplementary Material Sections 7.6 and 7.7). The largest source of uncertainty in calculations of P^{v}_{sat} are the carbonate solubilities and their significant dependence

511 on major element composition of the melt and errors on measurements of CO_2-eq (and H_2O-eq)
512 concentration, which can dwarf variations due to f_{O2} and S (Supplementary Material Figure S17).
513 Despite these uncertainties, we are confident that our modeling captures the overall trends in the
514 effects of S and f_{O2} on calculations of P^v_{sat} and ΔP^v_{sat} for basaltic melt compositions (see
515 Supplementary Material Section 7.2). We describe these potential limitations of our model in
516 detail in Supplementary Material Section 7.

517 As emphasized in the Introduction, values of P^v_{sat} are routinely and widely calculated based
518 on the volatile contents of glasses to provide minimum estimates of the P at which the volatile
519 contents were set (e.g., Anderson *et al.* 1989; Blundy and Cashman 2008; Colman *et al.* 2015;
520 Wanless *et al.* 2015; Camejo-Harry *et al.* 2018, 2019; Black and Andrews 2020; Wieser *et al.*
521 2021). With advances in microanalysis, melt inclusion and matrix glass studies are increasingly
522 co-determining the concentrations of a more complete suite of volatiles in the samples (H, C, S,
523 Cl, F, etc.) and Fe^{3+}/Fe_T and/or S^{6+}/S_T to constrain f_{O2}. However, few such calculations of P^v_{sat}
524 include the effects of dissolved S or f_{O2} (e.g., Carroll and Webster 1994; Newman and
525 Lowenstern 2002; Lesne *et al.* 2015; Iacovino *et al.* 2021; Yip *et al.* 2022).

526 To investigate the magnitude of these effects in nature, we collated literature data on glassy
527 melt inclusions and matrix glasses where CO_2, H_2O, S, and Fe^{3+}/Fe_T have been measured for the
528 same glass sample. We have restricted our compilation to low-alkali basaltic glass compositions
529 similar to the Hawaiian tholeiite we have adopted as a reference as the carbonate solubility is
530 highly dependent on melt composition and is fixed in these calculations (e.g., Supplementary
531 Material Figure S15). However, to examine magmas formed at the low f_{O2} extreme of our
532 calculations we include lunar and martian samples. These have much higher FeO than a
533 Hawaiian tholeiite and hence the carbonate solubility function we use here may not be

appropriate. For each terrestrial glass sample included in our compilation, we calculate P^{v}_{sat} at T = 1200 °C using the known f_{O2} based on measured Fe^{3+}/Fe_T ratios and measured melt composition (which can influence C_{*S2-} and C_{SO42-} in our model, but not other solubilities). For lunar and martian glasses, we calculate P^{v}_{sat} using a range of f_{O2} appropriate for these magmas (-5 < ΔFMQ < -1; e.g., Shearer *et al.* 2006; Gaillard *et al.* 2021). As well as P^{v}_{sat}, we also calculate the vapor composition in equilibrium with the measure melt composition at P^{v}_{sat}: we do not discuss the vapor composition in the main text, but this can be found in Supplementary Material Section 8. Calculated vapor compositions could be compared to natural volcanic gas samples and fluid inclusions or used to reconstruct bulk melt inclusion compositions when a bubble is present.

Most modern terrestrial magmas have f_{O2} levels corresponding to -1 ≲ ΔFMQ ≲ +2 (e.g., Cottrell *et al.* 2021) and contain significant S (typically 900–1200 ppm S for MORBs, 1100–6000 ppm S for intraplate hotspots, and 1200–7000 for arcs; Wallace and Edmonds 2011; Gaillard *et al.* 2021). Hence, the SS^{min}, which for our calculations is between +1 ≲ ΔFMQ ≲ +2 (Figure 1) could influence calculated P^{v}_{sat} values for hotspot and arc magmas that have f_{O2} values overlapping the calculated range of the SS^{min}. The build-up of relatively insoluble reduced C-O-H species in the vapor described previously (Figure 1) is unlikely to be important for typical terrestrial magmas but is likely to be important for extra-terrestrial settings. Although we also discuss values of absolute P^{v}_{sat}, we focus on ΔP^{v}_{sat}, the difference between P^{v}_{sat} for full C-O-H-S-bearing system and the P^{v}_{sat} value for the oxidized C-O-H reference (i.e., case 1, which has been used widely in existing calculations of P^{v}_{sat}).

This is the peer-reviewed, final accepted version for American Mineralogist, published by the Mineralogical Society of America.
The published version is subject to change. Cite as Authors (Year) Title. American Mineralogist, in press.
DOI: https://doi.org/10.2138/am-2022-8739. http://www.minsocam.org/

4.1 Mid-ocean ridge basalts

Figure 6a–c shows measured volatile contents and calculated P^{v}_{sat} and ΔP^{v}_{sat} for MORB submarine matrix glasses. These MORBs have an $f_{O2} \leq$ ΔFMQ+0.4, so their calculated values of P^{v}_{sat} are relatively insensitive to f_{O2} and S at the S contents observed ($\Delta P^{v}_{sat} \leq$ 33 bars, Figure 6c). Thus, calculations of P^{v}_{sat} for MORB that do not include the effects of f_{O2} and S would only underestimate P^{v}_{sat} by $\lesssim$ 30 bars (Figure 6c). Reykjanes Ridge glasses have low CO_2 and H_2O concentrations due to degassing to shallow depths (≤100 ppm CO_2-eq and ≤0.3 wt% H_2O-eq; Figure 6a; e.g., Nichols *et al.*, 2002), but they have not degassed significant S (~1200 ppm S-eq, Figure 6b; e.g., Nichols *et al.* 2002; Shorttle *et al.* 2015) and their f_{O2} is roughly where the SS^{min} can start to affect P^{v}_{sat} (Figure 6b). The combination of relatively high f_{O2} and S_T and low H_T and C_T leads to large values of $\Delta P^{v}_{sat}/P^{v}_{sat}$ (i.e., 10–40% based on the lines of constant $100*(\Delta P^{v}_{sat}/\Delta P^{v}_{sat})$ shown in Figure 6c). Thus, including the effects of S and f_{O2} in calculations of P^{v}_{sat} result in only small absolute values of ΔP^{v}_{sat}, but when compared to the low P^{v}_{sat} (due the low CO_2-H_2O abundances) this leads to a large relative effect on ΔP^{v}_{sat} (i.e., 10–40%; Figure 6c).

4.2 Ocean island basalts

Basalts related to hotspots have an f_{O2} range that straddles the SS^{min} calculated for the reference basalt used in this study (e.g., ΔFMQ+1 to +3 using global compilations; Moussallam *et al.* 2019; Cottrell *et al.* 2021) and can have much higher S_T contents than MORB glasses (e,g,, Ding and Dasgupta 2018). Hence S could significantly influence calculated values of P^{v}_{sat}. The broad positive correlation between S and f_{O2} seen in Figure 6e (and also h for Marianas samples) is caused by progressive reduction during S degassing (e.g., Anderson and Wright 1972; Carmichael and Ghiorso 1986; Burgisser and Scaillet 2007; Métrich *et al.* 2009; Gaillard *et al.*

579 2011, 2015; Kelley and Cottrell 2012; Moussallam *et al.* 2014, 2016; Brounce *et al.* 2017). Due
580 to the f_{O2} range of the submarine matrix glasses from Mauna Kea and melt inclusion data from
581 Kīlauea, and their low H_2O and CO_2 concentrations (<240 ppm CO_2-eq and ≤0.81 wt% H_2O-eq;
582 Figure 6d), the calculated ΔP^{v}_{sat} is up to 150 bars (the yellow symbols in Figure 6f). Both these
583 factors enhance the effect of the SS^{min} on calculated P^{v}_{sat}, leading to relatively large absolute and
584 relative differences in P^{v}_{sat} (i.e., ΔP^{v}_{sat} = 30–120 bars such that the relative effect is 20–60%;
585 Figure 6e and f).

586 Melt inclusions from Iceland also show the effect of elevated f_{O2} on absolute differences in ΔP^{v}_{sat}
587 (Figure 6i), but a smaller effect on the relative increase in P^{v}_{sat} (i.e., ΔP^{v}_{sat} is <20% of the value
588 of P^{v}_{sat}; Figure 6f). This is due to the higher CO_2 concentrations of the Icelandic melt inclusions
589 (Figure 6d). Given the dominant influence of CO_2 on P^{v}_{sat} in these water-poor samples, P^{v}_{sat} for
590 the Icelandic samples is generally higher than for the Hawaiian samples. Thus, while the increase
591 in P^{v}_{sat} (which is approximately equal to ΔP^{v}_{sat}) is similar (several 10's of bars) for the most
592 oxidized samples from both groups as they approach the SS^{min}, when normalized to the absolute
593 value of P^{v}_{sat}, the percentage increase in P^{v}_{sat} for the most oxidized sample of the two sets of
594 OIBs is smaller for the Icelandic samples (20% rather than 60%). This is likely a general rule:
595 although ΔP^{v}_{sat} is similar in deeply trapped melt inclusions that have not experienced significant
596 degassing of CO_2 and H_2O relative to shallowly trapped melt inclusions/matrix glasses, the
597 relative effect on ΔP^{v}_{sat} will be lower in deep, undegassed melts than in shallow, degassed melts
598 (Figure 6f).

599

4.3 Arc basalts

Melt inclusion and matrix glasses from basalts from the Marianas arc have f_{O2} values on the low f_{O2}-limb of the SS^{min} (Figure 6h). Thus, similar to OIB-related melt inclusions, arc-related melt inclusions with sufficient S also show higher calculated values of ΔP^{v}_{sat} with increasing f_{O2} as S-bearing species contribute progressively more to the value of P^{v}_{sat}. For the Marianas samples, H_2O and CO_2 positively correlate and the CO_2 concentrations are high (Figure 6g). For the melt inclusions, this results in the negative correlation of ΔP^{v}_{sat} with P^{v}_{sat} (Figure 6i), reflecting the larger impact of S in the f_{O2} range of arc magmas when H_2O and CO_2 contents are lowest (see Section 3.2). The matrix glasses do not show this trend because of their lower f_{O2} and S (Figure 6h and i). However, as also observed for OIBs, ΔP^{v}_{sat} is small relative to P^{v}_{sat} (relative effect on $\Delta P^{v}_{sat} \lesssim 20\%$, and mostly $\lesssim 10\%$ for melt inclusions and matrix glasses from the Marianas samples; Figure 6i) due to their overall high CO_2 and H_2O contents (Figure 6g). Conversely, matrix glasses from the Bonin islands are too reduced for the SS^{min} to be important and therefore ΔP^{v}_{sat} is small (blue diamonds in Figure 6h and i).

4.4 Lunar and martian basalts

Lunar and martian basalts formed and evolved under significantly reduced conditions relative to modern terrestrial settings, with an f_{O2} range of $-5 \lesssim \Delta FMQ \lesssim -1$ (e.g., Shearer *et al.* 2006; Gaillard *et al.* 2021). As has been pointed out previously (e.g., Section 3.2.1; Scaillet and Pichavant 2004; Wetzel *et al.* 2015; Newcombe *et al.* 2017; Lo *et al.* 2021), not including the effects of f_{O2} as an independent variable can lead to significant underestimations in P^{v}_{sat} at the

low f_{O2} experienced by lunar and martian magmas due to the low solubility of reduced C-O-H species. Calculated P^{v}_{sat} is very sensitive to f_{O2} in this f_{O2} range, so accurate f_{O2} estimates are vital for accurate P^{v}_{sat} estimates. Additionally, primary magmas from both bodies are estimated to contain non-negligible S (up to ~900 and ~3500 ppm S-eq for the Moon and Mars, respectively, e.g., Gaillard *et al.* 2021). However, given that the SS^{min} is only likely to be observed at more oxidising conditions than those prevalent on the Moon or Mars, this effect is unlikely to be important. However, the low H and C concentrations of these magmas ($\lesssim$1500 ppm H_2O and $\lesssim$ 6 ppm CO_2 in lunar melt inclusions; $\lesssim$ 2000 ppm H_2O and $\lesssim$ 200 ppm CO_2 in Martian magmas; Gaillard *et al.* 2021; Saal and Hauri 2021) suggest that S-bearing species could be an important component of the vapor released by lunar and martian magmas on ascent.

Usui *et al.* (2012) and Saal and Hauri (2021) analyzed CO_2-eq, H_2O-eq, and S-eq in melt inclusions and matrix glasses from martian and lunar samples (Figure 7a and b), but no measurements or estimates of f_{O2} are available for the glasses. Hence, we calculated P^{v}_{sat} values for each glass at f_{O2} values spanning the range $-5 < \Delta FMQ < -1$ at 1200°C (e.g., Herd *et al.* 2002; Shearer *et al.* 2006), which generates the curves shown in Figure 7c and d (each curve is for a single analysed glass). The range in ΔP^{v}_{sat} from Figure 7c and d are shown as vertical lines in Figure 7e and f. For both lunar and martian samples, H_2O-eq < 0.2 wt% but the lunar samples have low CO_2-eq (<16 ppm) and S-eq (900 ppm) relative to the martian samples (<240 ppm CO_2-eq and <3500 ppm S-eq) (Figure 7a and b). The lunar samples record low pressures (i.e., P^{v}_{sat} < 50 bars; Figure 7c and e), and excluding S and reduced C-O-H species leads to underestimates of P^{v}_{sat} by up to 130% at ΔFMQ-5 (Figure 7e). The martian samples record much higher pressures but the relative change in P^{v}_{sat} by including S and reduced C-O-H species is still large, up to 100% at ΔFMQ-5 (Figure 6p). Based on our calculations, neither sulfide- nor

graphite-saturation is indicated for lunar samples but most of our calculations for martian samples suggest sulfide (and sometimes graphite) saturation are reached; in such cases, the calculated equilibrium between melt and vapor is metastable, indicated by dashed curves (Figure 7d and f). Care must be taken applying these results as the carbonate solubility used may not be applicable to lunar and martian compositions (although sulfide and sulfate solubilities are appropriate).

Our results are in general agreement with Wetzel *et al.* (2015) and Newcombe *et al.* (2017a), who calculated P^{v}_{sat} for lunar glasses including reduced C-O-H species in the system: OH^{-}, H_2O_{mol}, and $Fe(CO)_5$ in the melt and CO and H_2O in the vapor (Wetzel *et al.* 2015); and OH^{-}, CO_3^{2-}, and CO in the melt and H_2, H_2O, CO, and CO_2 in the vapor (Newcombe *et al.* 2017a). In general, this highlights that modelling lunar and martian magmas requires inclusion of both reduced and oxidised C-O-H-S species (Newcombe *et al.* 2017a) and this will have implications for where magmas are stored and eruption dynamics (e.g., Lo *et al.* 2021). Also, these calculations of P^{v}_{sat} are highly-dependent on the f_{O2} used to calculate P^{v}_{sat} and accurate f_{O2} estimates are needed for accurate P^{v}_{sat} estimates (e.g., Figure 7e and f). However, quantitative results are sensitive to the solubilities in the melt of the reduced species, and more work is necessary to ensure their accuracy, but the trends shown here are robust.

5 Acknowledgements

ECH was funded by a Caltech Geology Option Post-Doctoral Fellowship and a Caltech Centre for Comparative Planetary Evolution (^{3}CPE) research grant, and is supported by the New Zealand Ministry of Business, Innovation and Employment (MBIE) through the Hazards and

667 Risk Management and New Zealand Geothermal Futures programme (Strategic Science
668 Investment Fund, contract C05X1702). PL is funded by an Embiricos Trust scholarship from
669 Jesus College, University of Cambridge.

6 References

Allabar, A. and Nowak, M. 2018. Message in a bottle: Spontaneous phase separation of hydrous Vesuvius melt even at low decompression rates. *Earth and Planetary Science Letters*, **501**, 192–201, https://doi.org/10.1016/J.EPSL.2018.08.047.

Allison, C.M., Roggensack, K. and Clarke, A.B. 2019. H2O–CO2 solubility in alkali-rich mafic magmas: new experiments at mid-crustal pressures. *Contributions to Mineralogy and Petrology*, **174**, 58, https://doi.org/10.1007/s00410-019-1592-4.

Allison, C.M., Roggensack, K. and Clarke, A.B. 2022. MafiCH: a general model for H2O–CO2 solubility in mafic magmas. *Contributions to Mineralogy and Petrology*, **177**, 1–22, https://doi.org/10.1007/S00410-022-01903-Y/FIGURES/10.

Anderson, A.T.J. 1974. Evidence for a Picritic, Volatile-rich Magma beneath Mt. Shasta, California. *Journal of Petrology*, **15**, 243–267, https://doi.org/10.1093/PETROLOGY/15.2.243.

Anderson, A.T.J. and Brown, G.G. 1993. CO2 contents and formation pressures of some Kilauean melt inclusions. *American Mineralogist*, **78**, 794–803.

Anderson, A.T.J. and Wright, T.L. 1972. Phenocrysts and glass inclusions and their bearing on oxidation and mixing of basaltic magmas, kilauea volcano, hawaii. *American Mineralogist*, **57**, 188–216.

Anderson, A.T.J., Newman, S., Williams, S.N., Druitt, T.H., Skirius, C. and Stolper, E.M. 1989a. H2O, CO2, CI, and gas in Plinian and ash-flow Bishop rhyolite. *Geology*, **17**, 221–225.

Anderson, A.T.J., Newman, S., Williams, S.N., Druitt, T.H., Skirius, C. and Stolper, E.M. 1989b. H2O, CO2, CI, and gas in Plinian and ash-flow Bishop rhyolite. *Geology*, **17**, 221–225, https://doi.org/10.1130/0091-7613(1989)017.

Ardia, P., Hirschmann, M.M., Withers, A.C. and Stanley, B.D. 2013. Solubility of CH4 in a synthetic basaltic melt, with applications to atmosphere–magma ocean–core partitioning of volatiles and to the evolution of the Martian atmosphere. *Geochimica et Cosmochimica Acta*, **114**, 52–71, https://doi.org/10.1016/J.GCA.2013.03.028.

Armstrong, L.S., Hirschmann, M.M., Stanley, B.D., Falksen, E.G. and Jacobsen, S.D. 2015. Speciation and solubility of reduced C-O-H-N volatiles in mafic melt: Implications for volcanism, atmospheric evolution, and deep volatile cycles in the terrestrial planets. *Geochimica et Cosmochimica Acta*, **171**, 283–302, https://doi.org/10.1016/j.gca.2015.07.007.

Aubaud, C. 2022. Carbon stable isotope constraints on CO2 degassing models of ridge, hotspot and arc magmas. *Chemical Geology*, **605**, 120962, https://doi.org/10.1016/J.CHEMGEO.2022.120962.

Backnaes, L. and Deubener, J. 2011. Experimental studies on sulfur solubility in silicate melts at

706 near-atmospheric pressure. *Reviews in Mineralogy and Geochemistry*, **73**, 143–165,
707 https://doi.org/10.2138/rmg.2011.73.6.

708 Baker, D.R. and Moretti, R. 2011. Modeling the Solubility of Sulfur in Magmas: A 50-Year Old
709 Geochemical Challenge. *Reviews in Mineralogy and Geochemistry*, **73**, 167–213,
710 https://doi.org/10.2138/RMG.2011.73.7.

711 Baumgartner, R.J., Baratoux, D., Gaillard, F. and Fiorentini, M.L. 2017. Numerical modelling of
712 erosion and assimilation of sulfur-rich substrate by martian lava flows: Implications for the
713 genesis of massive sulfide mineralization on Mars. *Icarus*, **296**, 257–274,
714 https://doi.org/10.1016/j.icarus.2017.06.016.

715 Behrens, H. and Nowak, M. 2010. Quantification of H2O Speciation in Silicate Glasses and
716 Melts by IR Spectroscopy - in situ versus Quench Techniques.
717 *http://dx.doi.org/10.1080/0141159031000076048*, **76**, 45–61,
718 https://doi.org/10.1080/0141159031000076048.

719 Belgrano, T.M., Tollan, P.M., Marxer, F. and Diamond, L.W. 2021. Paleobathymetry of
720 Submarine Lavas in the Samail and Troodos Ophiolites: Insights From Volatiles in Glasses
721 and Implications for Hydrothermal Systems. *Journal of Geophysical Research: Solid Earth*,
722 **126**, e2021JB021966, https://doi.org/10.1029/2021JB021966.

723 Black, B.A. and Andrews, B.J. 2020. Petrologic imaging of the architecture of magma reservoirs
724 feeding caldera-forming eruptions. *Earth and Planetary Science Letters*, **552**, 116572,
725 https://doi.org/10.1016/J.EPSL.2020.116572.

726 Blank, J.G. and Brooker, R.A. 1994. Experimental studies of carbon dioxide in silicate melts:
727 Solubility, speciation, and stable carbon isotope behaviour. *Reviews in Mineralogy and*
728 *Geochemistry*, **30**, 157–186.

729 Blundy, J.D. and Cashman, K.V. 2008. Petrologic reconstruction of magmatic system variables
730 and processes. *Reviews in Mineralogy and Geochemistry*, **69**, 179–239.

731 Boulliung, J. and Wood, B.J. 2022. SO2 solubility and degassing behavior in silicate melts.
732 *Geochimica et Cosmochimica Acta Volume , 1 November 2022, Pages 150-164*, **336**, 150–
733 164, https://doi.org/10.1016/j.gca.2022.08.032.

734 Brooker, R.A., Kohn, S.C., Holloway, J.R., McMillan, P.F. and Carroll, M.R. 1999. Solubility,
735 speciation and dissolution mechanisms for CO2 in melts on the NaAlO2-SiO2 join.
736 *Geochimica et Cosmochimica Acta*, **63**, 3549–3565.

737 Brounce, M.N., Kelley, K.A. and Cottrell, E. 2014. Variations in Fe3+/∑Fe of Mariana Arc
738 Basalts and Mantle Wedge fO2. *Journal of Petrology*, **55**, 2513–2536,
739 https://doi.org/10.1093/PETROLOGY/EGU065.

740 Brounce, M.N., Kelley, K.A., Stern, R., Martinez, F. and Cottrell, E. 2016. The Fina Nagu
741 volcanic complex: Unusual submarine arc volcanism in the rapidly deforming southern
742 Mariana margin. *Geochemistry, Geophysics, Geosystems*, **17**, 4078–4091,

https://doi.org/10.1002/2016GC006457.

Brounce, M.N., Stolper, E.M. and Eiler, J. 2017. Redox variations in Mauna Kea lavas, the oxygen fugacity of the Hawaiian plume, and the role of volcanic gases in Earth's oxygenation. *Proceedings of the National Academy of Sciences of the United States of America*, **114**, https://doi.org/10.1073/pnas.1619527114.

Brounce, M.N., Reagan, M.K., Kelley, K.A., Cottrell, E., Shimizu, K. and Almeev, R. 2021. Covariation of Slab Tracers, Volatiles, and Oxidation During Subduction Initiation. *Geochemistry Geophysics Geosystems*, **22**, e2021GC009823, https://doi.org/https://doi.org/10.1029/2021GC009823.

Bucholz, C.E., Gaetani, G.A., Behn, M.D. and Shimizu, N. 2013. Post-entrapment modification of volatiles and oxygen fugacity in olivine-hosted melt inclusions. *Earth and Planetary Science Letters*, **374**, 145–155, https://doi.org/10.1016/j.epsl.2013.05.033.

Burgisser, A. and Scaillet, B. 2007. Redox evolution of a degassing magma rising to the surface. *Nature*, **445**, 194–197, https://doi.org/10.1038/nature05509.

Burgisser, A., Alletti, M. and Scaillet, B. 2015. Simulating the behavior of volatiles belonging to the C–O–H–S system in silicate melts under magmatic conditions with the software D-Compress. *Computers & Geosciences*, **79**, 1–14, https://doi.org/10.1016/J.CAGEO.2015.03.002.

Burnham, C.W. 1979. The importance of volatile constituents. *In*: Yoder Jr, H. S. (ed.) *The Evolution of the Igneous Rocks: Fiftieth Anniversary Perspectives*. 439–482.

Burnham, C.W. and Davis, N.F. 1974. The role of H 2 O in silicate melts; II, Thermodynamic and phase relations in the system NaAlSi 3 O 8 -H 2 O to 10 kilobars, 700 degrees to 1100 degrees C. *American Journal of Science*, **274**, 902–940, https://doi.org/10.2475/AJS.274.8.902.

Camejo-Harry, M., Melekhova, E., Blundy, J., Attridge, W., Robertson, R. and Christopher, T. 2018. Magma evolution beneath Bequia, Lesser Antilles, deduced from petrology of lavas and plutonic xenoliths. *Contributions to Mineralogy and Petrology*, **173**, 1–26, https://doi.org/10.1007/S00410-018-1504-Z/FIGURES/14.

Camejo-Harry, M., Melekhova, E., Blundy, J. and Robertson, R. 2019. Evolution in magma storage conditions beneath Kick-'em-Jenny and Kick-'em-Jack submarine volcanoes, Lesser Antilles arc. *Journal of Volcanology and Geothermal Research*, **373**, 1–22, https://doi.org/10.1016/J.JVOLGEORES.2019.01.023.

Caricchi, L., Sheldrake, T.E. and Blundy, J.D. 2018. Modulation of magmatic processes by CO2 flushing. *Earth and Planetary Science Letters*, **491**, 160–171, https://doi.org/10.1016/j.epsl.2018.03.042.

Carmichael, I.S.E. and Ghiorso, M.S. 1986. Oxidation-reduction relations in basic magma: a case for homogeneous equilibria. *Earth and Planetary Science Letters*, **78**, 200–210,

https://doi.org/10.1016/0012-821X(86)90061-0.

Carroll, M.R. and Rutherford, M.J. 1985. Sulfide and sulfate saturation in hydrous silicate melts. *Journal of Geophysical Research: Solid Earth*, **90**, C601–C612, https://doi.org/10.1029/JB090IS02P0C601.

Carroll, M.R. and Rutherford, M.J. 1988. Sulfur speciation in hydrous experimental glasses of varying oxidation state; results from measured wavelength shifts of sulfur X-rays | American Mineralogist | GeoScienceWorld. *American Mineralogist*, **73**, 845–849.

Carroll, M.R. and Webster, J.D. 1994. Solubilities of sulfur, noble gases, nitrogen, chlorine, and fluorine in magmas. *Volatiles in Magmas*, 231–280, https://doi.org/10.1515/9781501509674-013.

Cicconi, M.R., Le Losq, C., Moretti, R. and Neuville, D.R. 2020. Magmas are the Largest Repositories and Carriers of Earth's Redox Processes. *Elements*, **16**, 173–178, https://doi.org/10.2138/GSELEMENTS.16.3.173.

Clemente, B., SCAILLET, B. and PICHAVANT, M. 2004. The Solubility of Sulphur in Hydrous Rhyolitic Melts. *Journal of Petrology*, **45**, 2171–2196, https://doi.org/10.1093/petrology/egh052.

Colman, A., Sinton, J.M. and Wanless, V.D. 2015. Constraints from melt inclusions on depths of magma residence at intermediate magma supply along the Galápagos Spreading Center. *Earth and Planetary Science Letters*, **412**, 122–131, https://doi.org/10.1016/J.EPSL.2014.12.007.

Coombs, M.L., Sisson, T.W. and Lipman, P.W. 2006. Growth history of Kilauea inferred from volatile concentrations in submarine-collected basalts. *Journal of Volcanology and Geothermal Research*, **151**, 19–49, https://doi.org/10.1016/J.JVOLGEORES.2005.07.037.

Cottrell, E., Birner, S.K., Brounce, M.N., Davis, F.A., Waters, L.E. and Kelley, K.A. 2021. Oxygen Fugacity Across Tectonic Settings. *In*: Moretti, R. and Neuville, D. R. (eds) *Magma Redox Geochemistry*. 33–61., https://doi.org/10.1002/9781119473206.CH3.

Coulthard Jr, D.A., Reagan, M.K., et al. 2022. Magma Source Evolution Following Subduction Initiation: Evidence From the Element Concentrations, Stable Isotope Ratios, and Water Contents of Volcanic Glasses From the Bonin Forearc (IODP Expedition 352). *Geochemistry Geophysics Geosystems*, **1**, e2020GC009054, https://doi.org/https://doi.org/10.1029/2020GC009054.

Ding, S. and Dasgupta, R. 2018. Sulfur Inventory of Ocean Island Basalt Source Regions Constrained by Modeling the Fate of Sulfide during Decompression Melting of a Heterogeneous Mantle. *Journal of Petrology*, **59**, 1281–1308, https://doi.org/10.1093/PETROLOGY/EGY061.

Dingwell, D.B. and Webb, S.L. 1990. Relaxation in silicate melts. *European Journal of Mineralogy*, **2**, 427–449.

817 Dixon, J.E. and Stolper, E.M. 1995. An experimental study water and carbon dioxide solubilities
818 in mid-ocean ridge basaltic liquids. Part II: Application to degassing. *Journal of Petrology*,
819 **36**, 1633–1646.

820 Dixon, J.E., Stolper, E.M. and Delaney, J.R. 1988. Infrared spectroscopic measurements of CO2
821 and H2O in the Juan de Fuca Ridge basaltic glasses. *Earth and Planetary Science Letters*,
822 **90**, 87–104.

823 Dixon, J.E., Stolper, E.M. and Holloway, J.R. 1995. An experimental study of water and carbon
824 dioxide solubilities in mid-ocean ridge basaltic liquids. Part I: Calibration and solubility
825 models. *Journal of Petrology*, **36**, 1607–1631,
826 https://doi.org/10.1093/oxfordjournals.petrology.a037267.

827 Duan, X. 2014. A general model for predicting the solubility behavior of H2O–CO2 fluids in
828 silicate melts over a wide range of pressure, temperature and compositions. *Geochimica et*
829 *Cosmochimica Acta*, **125**, 582–609, https://doi.org/10.1016/J.GCA.2013.10.018.

830 Fincham, C.J.B. and Richardson, F.D. 1954. The behaviour of sulphur in silicate and aluminate
831 melts. *Proceedings of the Royal Society of London. Series A. Mathematical and Physical*
832 *Sciences*, **223**, 40–62, https://doi.org/10.1098/rspa.1954.0099.

833 Fine, G. and Stolper, E.M. 1986. Dissolved carbon dioxide in basaltic glasses: Concentrations
834 and speciation. *Earth and Planetary Science Letters*, **76**, 263–278,
835 https://doi.org/10.1016/0012-821X(86)90078-6.

836 Gaetani, G.A., O'Leary, J.A., Shimizu, N., Bucholz, C.E. and Newville, M. 2012. Rapid
837 reequilibration of H2O and oxygen fugacity in olivine-hosted melt inclusions. *Geology*, **40**,
838 915–918, https://doi.org/10.1130/G32992.1.

839 Gaillard, F. and Scaillet, B. 2009. The sulfur content of volcanic gases on Mars. *Earth and*
840 *Planetary Science Letters*, **279**, 34–43, https://doi.org/10.1016/J.EPSL.2008.12.028.

841 Gaillard, F. and Scaillet, B. 2014. A theoretical framework for volcanic degassing chemistry in a
842 comparative planetology perspective and implications for planetary atmospheres. *Earth and*
843 *Planetary Science Letters*, **403**, 307–316, https://doi.org/10.1016/j.epsl.2014.07.009.

844 Gaillard, F., Schmidt, B., Mackwell, S. and McCammon, C. 2003. Rate of hydrogen–iron redox
845 exchange in silicate melts and glasses. *Geochimica et Cosmochimica Acta*, **67**, 2427–2441,
846 https://doi.org/10.1016/s0016-7037(02)01407-2.

847 Gaillard, F., Scaillet, B. and Arndt, N.T. 2011. Atmospheric oxygenation caused by a change in
848 volcanic degassing pressure. *Nature*, **478**, 229–232, https://doi.org/10.1038/nature10460.

849 Gaillard, F., Michalski, J., Berger, G., McLennan, S.M. and Scaillet, B. 2013. Geochemical
850 reservoirs and timing of sulfur cycling on Mars. *Space Science Reviews*, **174**, 251–300,
851 https://doi.org/10.1007/s11214-012-9947-4.

852 Gaillard, F., Scaillet, B., Pichavant, M. and Iacono-Marziano, G. 2015. The redox geodynamics

linking basalts and their mantle sources through space and time. *Chemical Geology*, **418**, 217–233, https://doi.org/10.1016/j.chemgeo.2015.07.030.

Gaillard, F., Bouhifd, M.A., et al. 2021. The Diverse Planetary Ingassing/Outgassing Paths Produced over Billions of Years of Magmatic Activity. *Space Science Reviews*, **217**, 1–54, https://doi.org/10.1007/S11214-021-00802-1/FIGURES/18.

Gardner, J.E., Wadsworth, F.B., Carley, T.L., Llewellin, E.W., Kusumaatmaja, H. and Sahagian, D. 2022. Bubble Formation in Magma. *https://doi.org/10.1146/annurev-earth-031621-080308*, **51**, https://doi.org/10.1146/ANNUREV-EARTH-031621-080308.

Ghiorso, M.S. and Gualda, G.A.R. 2015. An H2O–CO2 mixed fluid saturation model compatible with rhyolite-MELTS. *Contributions to Mineralogy and Petrology*, **169**, 53, https://doi.org/10.1007/s00410-015-1141-8.

Hartley, M.E., Neave, D.A., Maclennan, J., Edmonds, M. and Thordarson, T. 2015. Diffusive over-hydration of olivine-hosted melt inclusions. *Earth and Planetary Science Letters*, **425**, 168–178, https://doi.org/10.1016/J.EPSL.2015.06.008.

Hartley, M.E., Shorttle, O., Maclennan, J., Moussallam, Y. and Edmonds, M. 2017. Olivine-hosted melt inclusions as an archive of redox heterogeneity in magmatic systems. *Earth and Planetary Science Letters*, **479**, 192–205, https://doi.org/10.1016/J.EPSL.2017.09.029.

Herd, C.D.K., Borg, L.E., Jones, J.H. and Papike, J.J. 2002. Oxygen fugacity and geochemical variations in the martian basalts: implications for martian basalt petrogenesis and the oxidation state of the upper mantle of Mars. *Geochimica et Cosmochimica Acta*, **66**, 2025–2036, https://doi.org/10.1016/S0016-7037(02)00828-1.

Hirschmann, M.M., Withers, A.C., Ardia, P. and Foley, N.T. 2012. Solubility of molecular hydrogen in silicate melts and consequences for volatile evolution of terrestrial planets. *Earth and Planetary Science Letters*, **345**–**348**, 38–48, https://doi.org/10.1016/J.EPSL.2012.06.031.

Holloway, J.R. and Blank, J.G. 1994. Application of experimental results to C-O-H species in natural melts. *Reviews in Mineralogy and Geochemistry1*, **30**, 187–230.

Holloway, J.R., Pan, V. and Gudmundsson, G.B. 1992. High-pressure fluid-absent melting experiments in the presence of graphite: oxygen fugacity, ferric/ferrous ratio and dissolved CO2. *European Journal of Mineralogy*, **4**, 105–114.

Hughes, E.C., Saper, L.M., Liggins, P., O'Neill, H.S.C. and Stolper, E.M. 2023. The sulfur solubility minimum and maximum in silicate melt. *Journal of the Geological Society*.

Iacono-Marziano, G., Morizet, Y., Le Trong, E. and Gaillard, F. 2012. New experimental data and semi-empirical parameterization of H2O–CO2 solubility in mafic melts. *Geochimica et Cosmochimica Acta*, **97**, 1–23, https://doi.org/10.1016/J.GCA.2012.08.035.

Iacono-Marziano, G., Ferraina, C., Gaillard, F., Di Carlo, I. and Arndt, N.T. 2017. Assimilation

of sulfate and carbonaceous rocks: Experimental study, thermodynamic modeling and application to the Noril'sk-Talnakh region (Russia). *Ore Geology Reviews*, **90**, 399–413, https://doi.org/10.1016/J.OREGEOREV.2017.04.027.

Iacovino, K., Matthews, S., Wieser, P.E., Moore, G.M. and Bégué, F. 2021. VESIcal Part I: An open-source thermodynamic model engine for mixed volatile (O-) solubility in silicate melts. *Earth and Space Science*, e2020EA001584, https://doi.org/10.1029/2020EA001584.

Jendrzejewski, N., Trull, T.W., Pineau, F. and Javoy, M. 1997. Carbon solubility in Mid-Ocean Ridge basaltic melt at low pressures (250–1950 bar). *Chemical Geology*, **138**, 81–92, https://doi.org/10.1016/S0009-2541(96)00176-3.

Jugo, P.J., Wilke, M. and Botcharnikov, R.E. 2010. Sulfur K-edge XANES analysis of natural and synthetic basaltic glasses: Implications for S speciation and S content as function of oxygen fugacity. *Geochimica et Cosmochimica Acta*, **74**, 5926–5938, https://doi.org/10.1016/J.GCA.2010.07.022.

Kadik, A., Pineau, F., Litvin, Y., Jendrzejewski, N., Martinez, I. and Javoy, M. 2004. Formation of Carbon and Hydrogen Species in Magmas at Low Oxygen Fugacity. *Journal of Petrology*, **45**, 1297–1310, https://doi.org/10.1093/PETROLOGY/EGH007.

Katsura, T. and Nagashima, S. 1974. Solubility of sulfur in some magmas at 1 atmosphere. *Geochimica et Cosmochimica Acta*, **38**, 517–531, https://doi.org/10.1016/0016-7037(74)90038-6.

Kelley, K.A. and Cottrell, E. 2012. The influence of magmatic differentiation on the oxidation state of Fe in a basaltic arc magma. *Earth and Planetary Science Letters*, **329**–**330**, 109–121, https://doi.org/10.1016/j.epsl.2012.02.010.

Klimm, K., Kohn, S.C., O'Dell, L.A., Botcharnikov, R.E. and Smith, M.E. 2012. The dissolution mechanism of sulphur in hydrous silicate melts. I: Assessment of analytical techniques in determining the sulphur speciation in iron-free to iron-poor glasses. *Chemical Geology*, **322**–**323**, 237–249, https://doi.org/10.1016/J.CHEMGEO.2012.04.027.

Konschak, A. and Keppler, H. 2014. The speciation of carbon dioxide in silicate melts. *Contributions to Mineralogy and Petrology*, **167**, 1–13, https://doi.org/10.1007/S00410-014-0998-2/FIGURES/14.

Kress, V.C. and Carmichael, I.S.E. 1991. The compressibility of silicate liquids containing Fe2O3 and the effect of composition, temperature, oxygen fugacity and pressure on their redox states. *Contributions to Mineralogy and Petrology*, **108**, 82–92, https://doi.org/10.1007/BF00307328.

Kress, V.C., Ghiorso, M.S. and Lastuka, C. 2004. Microsoft EXCEL spreadsheet-based program for calculating equilibrium gas speciation in the C–O–H–S–Cl–F system. *Computers & Geosciences*, **30**, 211–214, https://doi.org/10.1016/J.CAGEO.2003.10.006.

Le Voyer, M., Cottrell, E., Kelley, K.A., Brounce, M.N. and Hauri, E.H. 2015. The effect of

primary versus secondary processes on the volatile content of MORB glasses: An example from the equatorial Mid-Atlantic Ridge (5°N–3°S). *Journal of Geophysical Research: Solid Earth*, **120**, 125–144, https://doi.org/10.1002/2014JB011160.

Le Voyer, M., Hauri, E.H., et al. 2019. Carbon Fluxes and Primary Magma CO2 Contents Along the Global Mid-Ocean Ridge System. *Geochemistry, Geophysics, Geosystems*, **20**, 1387–1424, https://doi.org/10.1029/2018GC007630.

Lesne, P., Scaillet, B., Pichavant, M., Iacono-Marziano, G. and Beny, J.M. 2011. The H2O solubility of alkali basaltic melts: An experimental study. *Contributions to Mineralogy and Petrology*, **162**, 133–151, https://doi.org/10.1007/S00410-010-0588-X/FIGURES/12.

Lesne, P., Scaillet, B. and Pichavant, M. 2015. The solubility of sulfur in hydrous basaltic melts. *Chemical Geology*, **418**, 104–116, https://doi.org/10.1016/J.CHEMGEO.2015.03.025.

Liggins, P., Shorttle, O. and Rimmer, P.B. 2020. Can volcanism build hydrogen-rich early atmospheres? *Earth and Planetary Science Letters*, **550**, 116546, https://doi.org/10.1016/J.EPSL.2020.116546.

Liggins, P., Jordan, S., Rimmer, P.B. and Shorttle, O. 2022. Growth and Evolution of Secondary Volcanic Atmospheres: I. Identifying the Geological Character of Hot Rocky Planets. *Journal of Geophysical Research: Planets*, **127**, e2021JE007123, https://doi.org/10.1029/2021JE007123.

Lo, M., La Spina, G., Joy, K.H., Polacci, M. and Burton, M. 2021. Determining the Effect of Varying Magmatic Volatile Content on Lunar Magma Ascent Dynamics. *Journal of Geophysical Research: Planets*, **126**, e2021JE006939, https://doi.org/10.1029/2021JE006939.

Lund, D.C., Seeley, E.I., Asimow, P.D., Lewis, M.J., McCart, S.E. and Mudahy, A.A. 2018. Anomalous Pacific-Antarctic Ridge Volcanism Precedes Glacial Termination 2. *Geochemistry, Geophysics, Geosystems*, **19**, 2478–2491, https://doi.org/10.1029/2017GC007341.

Maclennan, J. 2017. Bubble formation and decrepitation control the CO2 content of olivine-hosted melt inclusions. *Geochemistry, Geophysics, Geosystems*, **18**, 597–616, https://doi.org/10.1002/2016GC006633.

Matjuschkin, V., Blundy, J.D. and Brooker, R.A. 2016. The effect of pressure on sulphur speciation in mid- to deep-crustal arc magmas and implications for the formation of porphyry copper deposits. *Contributions to Mineralogy and Petrology*, **171**, 66, https://doi.org/10.1007/s00410-016-1274-4.

Matthews, S.J., Moncrieff, D.H.S. and Carroll, M.R. 1999. Empirical Calibration of the Sulphur Valence Oxygen Barometer from Natural and Experimental Glasses: Method and Applications. *Mineralogical Magazine*, **63**, 421–431, https://doi.org/10.1180/002646199548510.

963 Métrich, N. 2021. Redox State of Volatiles and Their Relationships with Iron in Silicate Melts.
964 215–232, https://doi.org/10.1002/9781119473206.CH11.

965 Métrich, N., Berry, A.J., O'Neill, H.S.C. and Susini, J. 2009. The oxidation state of sulfur in
966 synthetic and natural glasses determined by X-ray absorption spectroscopy. *Geochimica et*
967 *Cosmochimica Acta*, **73**, 2382–2399, https://doi.org/10.1016/J.GCA.2009.01.025.

968 Moretti, R. 2021. Ionic Syntax and Equilibrium Approach to Redox Exchanges in Melts: Basic
969 Concepts and the Case of Iron and Sulfur in Degassing Magmas. *In*: Moretti, R. and
970 Neuville, D. R. (eds) *Magma Redox Geochemistry, Geophysical Monograph Series*. 115–
971 138., https://doi.org/10.1002/9781119473206.CH6.

972 Moretti, R. and Ottonello, G. 2003. Polymerization and disproportionation of iron and sulfur in
973 silicate melts: Insights from an optical basicity-based approach. *In*: *Journal of Non-*
974 *Crystalline Solids*. 111–119., https://doi.org/10.1016/S0022-3093(03)00297-7.

975 Moretti, R. and Ottonello, G. 2005. Solubility and speciation of sulfur in silicate melts: The
976 Conjugated Toop-Samis-Flood-Grjotheim (CTSFG) model. *Geochimica et Cosmochimica*
977 *Acta*, **69**, 801–823, https://doi.org/10.1016/J.GCA.2004.09.006.

978 Moretti, R. and Papale, P. 2004. On the oxidation state and volatile behavior in multicomponent
979 gas-melt equilibria. *Chemical Geology*, **213**, 265–280,
980 https://doi.org/10.1016/j.chemgeo.2004.08.048.

981 Moretti, R., Papale, P. and Ottonello, G. 2003. A model for the saturation of C-O-H-S fluids in
982 silicate melts. *Geological Society, London, Special Publications*, **213**, 81–101,
983 https://doi.org/10.1144/GSL.SP.2003.213.01.06.

984 Moretti, R., Métrich, N., Arienzo, I., Di Renzo, V., Aiuppa, A. and Allard, P. 2018. Degassing
985 vs. eruptive styles at Mt. Etna volcano (Sicily, Italy). Part I: Volatile stocking, gas fluxing,
986 and the shift from low-energy to highly explosive basaltic eruptions. *Chemical Geology*,
987 **482**, 1–17, https://doi.org/10.1016/J.CHEMGEO.2017.09.017.

988 Morizet, Y., Kohn, S.C. and Brooker, R.A. 2001. Annealing experiments on CO2-bearing jadeite
989 glass: an insight into the true temperature dependence of CO2 speciation in silicate melts.
990 *Mineralogical Magazine*, **65**, 701–707, https://doi.org/10.1180/0026461016560001.

991 Moune, S., Holtz, F. and Botcharnikov, R.E. 2009. Sulphur solubility in andesitic to basaltic
992 melts: implications for Hekla volcano. *Contributions to Mineralogy and Petrology*, **157**,
993 691–707, https://doi.org/10.1007/s00410-008-0359-0.

994 Moussallam, Y., Oppenheimer, C., et al. 2014. Tracking the changing oxidation state of Erebus
995 magmas, from mantle to surface, driven by magma ascent and degassing. *Earth and*
996 *Planetary Science Letters*, **393**, 200–209, https://doi.org/10.1016/j.epsl.2014.02.055.

997 Moussallam, Y., Edmonds, M., Scaillet, B., Peters, N., Gennaro, M.E., Sides, I. and
998 Oppenheimer, C. 2016. The impact of degassing on the oxidation state of basaltic magmas:
999 A case study of Kīlauea volcano. *Earth and Planetary Science Letters*, **450**, 317–325,

https://doi.org/10.1016/j.epsl.2016.06.031.

Moussallam, Y., Longpré, M.-A., et al. 2019. Mantle plumes are oxidised. *Earth and Planetary Science Letters*, **527**, 115798, https://doi.org/10.1016/J.EPSL.2019.115798.

Mysen, B. 2013. Structure–property relationships of COHN-saturated silicate melt coexisting with COHN fluid: A review of in-situ, high-temperature, high-pressure experiments. *Chemical Geology*, **346**, 113–124, https://doi.org/10.1016/J.CHEMGEO.2012.10.006.

Mysen, B.O., Virgo, D., Harrison, W.J. and Scarfe, C.M. 1980. Solubility mechanisms of H2O in silicate melts at high pressures and temperatures: a Raman spectroscopic study | American Mineralogist | GeoScienceWorld. *American Mineralogist*, **65**, 900–914.

Mysen, B.O., Kumamoto, K., Cody, G.D. and Fogel, M.L. 2011. Solubility and solution mechanisms of C–O–H volatiles in silicate melt with variable redox conditions and melt composition at upper mantle temperatures and pressures. *Geochimica et Cosmochimica Acta*, **75**, 6183–6199, https://doi.org/10.1016/J.GCA.2011.07.035.

Nash, W.M., Smythe, D.J. and Wood, B.J. 2019. Compositional and temperature effects on sulfur speciation and solubility in silicate melts. *Earth and Planetary Science Letters*, **507**, 187–198, https://doi.org/10.1016/J.EPSL.2018.12.006.

Newcombe, M.E., Brett, A., et al. 2017a. Solubility of water in lunar basalt at low pH2O. *Geochimica et Cosmochimica Acta*, **200**, 330–352, https://doi.org/10.1016/J.GCA.2016.12.026.

Newcombe, M.E., Brett, A., et al. 2017b. Solubility of water in lunar basalt at low pH2O. *Geochimica et Cosmochimica Acta*, **200**, 330–352, https://doi.org/10.1016/J.GCA.2016.12.026.

Newman, S. and Lowenstern, J.B. 2002. VolatileCalc: a silicate melt–H2O–CO2 solution model written in Visual Basic for excel. *Computers & Geosciences*, **28**, 597–604, https://doi.org/10.1016/S0098-3004(01)00081-4.

Nichols, A.R.L., Carroll, M.R. and Höskuldsson, Á. 2002. Is the Iceland hot spot also wet? Evidence from the water contents of undegassed submarine and subglacial pillow basalts. *Earth and Planetary Science Letters*, **202**, 77–87, https://doi.org/10.1016/S0012-821X(02)00758-6.

O'Neill, H.S.C. 2021. The thermodynamic controls on sulfide saturation in silicate melts with application to Ocean Floor Basalts. *In*: Moretti, R. and Neuville, D. R. (eds) *Magma Redox Geochemistry, Geophysical Monograph Series*. 177–213., https://doi.org/10.1002/9781119473206.ch10.

O'Neill, H.S.C. and Mavrogenes, J.A. 2002. The sulfide capacity and the sulfur content at sulfide saturation of silicate melts at 1400°C and 1 bar. *Journal of Petrology*, **43**, 1049–1087, https://doi.org/10.1093/petrology/43.6.1049.

1036 O'Neill, H.S.C. and Mavrogenes, J.A. 2022. The sulfate capacities of silicate melts. *Geochimica*
1037 *et Cosmochimica Acta*, https://doi.org/10.1016/J.GCA.2022.06.020.

1038 Papale, P., Moretti, R. and Barbato, D. 2006. The compositional dependence of the saturation
1039 surface of H2O+CO2 fluids in silicate melts. *Chemical Geology*, **229**, 78–95,
1040 https://doi.org/10.1016/j.chemgeo.2006.01.013.

1041 Papale, P., Moretti, R. and Paonita, A. 2022. Thermodynamics of Multi-component Gas–Melt
1042 Equilibrium in Magmas: Theory, Models, and Applications. *Reviews in Mineralogy and*
1043 *Geochemistry*, **87**, 431–556, https://doi.org/10.2138/RMG.2022.87.10.

1044 Paris, E., Giuli, G., Carroll, M.R. and Davoli, I. 2001. The valence and speciation of sulfur in
1045 glasses by X-ray absorption spectroscopy. *The Canadian Mineralogist*, **39**, 331–339,
1046 https://doi.org/10.2113/gscanmin.39.2.331.

1047 Portnyagin, M., Almeev, R., Matveev, S. and Holtz, F. 2008. Experimental evidence for rapid
1048 water exchange between melt inclusions in olivine and host magma. *Earth and Planetary*
1049 *Science Letters*, **272**, 541–552, https://doi.org/10.1016/J.EPSL.2008.05.020.

1050 Rasmussen, D.J., Plank, T.A., Wallace, P.J., Newcombe, M.E. and Lowenstern, J.B. 2020.
1051 Vapor-bubble growth in olivine-hosted melt inclusions. *American Mineralogist*, **105**, 1898–
1052 1919, https://doi.org/10.2138/am-2020-7377.

1053 Roedder, E. 1979. Origin and significance of magmatic inclusions. *Bulletin de Mineralogie*, **102**,
1054 487–510.

1055 Saal, A.E. and Hauri, E.H. 2021. Large sulfur isotope fractionation in lunar volcanic glasses
1056 reveals the magmatic differentiation and degassing of the Moon. *Science Advances*, **7**,
1057 eabe4641, https://doi.org/10.1126/sciadv.abe4641.

1058 Saal, A.E., Hauri, E.H., Langmuir, C.H. and Perfit, M.R. 2002. Vapour undersaturation in
1059 primitive mid-ocean-ridge basalt and the volatile content of Earth's upper mantle. *Nature*,
1060 **419**, 451–455, https://doi.org/10.1038/nature01073.

1061 Sahagian, D. and Carley, T.L. 2020. Explosive Volcanic Eruptions and Spinodal Decomposition:
1062 A Different Approach to Deciphering the Tiny Bubble Paradox. *Geochemistry, Geophysics,*
1063 *Geosystems*, **21**, e2019GC008898, https://doi.org/10.1029/2019GC008898.

1064 Scaillet, B. and Pichavant, M. 2004. Role of fO2 on fluid saturation in oceanic basalt. *Nature*
1065 *2004 430:6999*, **430**, 1–1, https://doi.org/10.1038/nature02814.

1066 Seaman, C., Sherman, S.B., Garcia, M.O., Baker, M.B., Balta, B. and Stolper, E.M. 2004.
1067 Volatiles in glasses from the HSDP2 drill core. *Geochemistry, Geophysics, Geosystems*, **5**,
1068 https://doi.org/10.1029/2003GC000596@10.1002/(ISSN)1525-2027.HAWI1.

1069 Shearer, C.K., Hess, P.C., et al. 2006. Thermal and Magmatic Evolution of the Moon. *Reviews in*
1070 *Mineralogy and Geochemistry*, **60**, 365–518, https://doi.org/10.2138/RMG.2006.60.4.

Shishkina, T.A., Botcharnikov, R.E., Holtz, F., Almeev, R.R., Jazwa, A.M. and Jakubiak, A.A. 2014. Compositional and pressure effects on the solubility of H2O and CO2 in mafic melts. *Chemical Geology*, **388**, 112–129, https://doi.org/10.1016/J.CHEMGEO.2014.09.001.

Shorttle, O., Moussallam, Y., Hartley, M.E., Maclennan, J., Edmonds, M. and Murton, B.J. 2015. Fe-XANES analyses of Reykjanes Ridge basalts: Implications for oceanic crust's role in the solid Earth oxygen cycle. *Earth and Planetary Science Letters*, **427**, 272–285, https://doi.org/10.1016/j.epsl.2015.07.017.

Silver, L.A. and Stolper, E.M. 1985. A Thermodynamic Model for Hydrous Silicate Melts. *The Journal of Geology*, **93**, 161–177, https://doi.org/10.1086/628938.

Soule, S.A., Nakata, D.S., Fornari, D.J., Fundis, A.T., Perfit, M.R. and Kurz, M.D. 2012. CO2 variability in mid-ocean ridge basalts from syn-emplacement degassing: Constraints on eruption dynamics. *Earth and Planetary Science Letters*, **327**–**328**, 39–49, https://doi.org/10.1016/J.EPSL.2012.01.034.

Spera, F.J. and Bergman, S.C. 1980. Carbon Dioxide in igneous petrogenesis: I. *Contributions to Mineralogy and Petrology*, **74**, 55–66, https://doi.org/10.1007/BF00375489.

Spilliaert, N., Allard, P., Métrich, N. and Sobolev, A. V. 2006. Melt inclusion record of the conditions of ascent, degassing, and extrusion of volatile-rich alkali basalt during the powerful 2002 flank eruption of Mount Etna (Italy). *Journal of Geophysical Research*, **111**, B04203, https://doi.org/10.1029/2005JB003934.

Stanley, B.D., Hirschmann, M.M. and Withers, A.C. 2014. Solubility of COH volatiles in graphite-saturated martian basalts. *Geochimica et Cosmochimica Acta*, **129**, 54–76, https://doi.org/10.1016/j.gca.2013.12.013.

Steele-Macinnis, M., Esposito, R. and Bodnar, R.J. 2011. Thermodynamic Model for the Effect of Post-entrapment Crystallization on the H2O-CO2 Systematics of Vapor-saturated, Silicate Melt Inclusions. *Journal of Petrology*, **52**, 2461–2482, https://doi.org/10.1093/petrology/egr052.

Stolper, E.M. 1982a. The speciation of water in silicate melts. *Geochimica et Cosmochimica Acta*, **46**, 2609–2620.

Stolper, E.M. 1982b. Water in silicate glasses: An infrared spectroscopic study. *Contributions to Mineralogy and Petrology 1982 81:1*, **81**, 1–17, https://doi.org/10.1007/BF00371154.

Stolper, E.M. 1989. Temperature dependence of the speciation of water in rhyolitic melts and glasses | American Mineralogist | GeoScienceWorld. *American Mineralogist*, **74**, 1247–1257.

Stolper, E.M. and Holloway, J.R. 1988. Experimental determination of the solubility of carbon dioxide in molten basalt at low pressure. *Earth and Planetary Science Letters*, **87**, 397–408, https://doi.org/10.1016/0012-821X(88)90004-0.

Sun, C. and Lee, C.-T.A. 2022. Redox evolution of crystallizing magmas with C-H-O-S volatiles and its implications for atmospheric oxygenation. *Geochimica et Cosmochimica Acta*, **338**, 302–321.

Thomas, R.W. and Wood, B.J. 2021. The chemical behaviour of chlorine in silicate melts. *Geochimica et Cosmochimica Acta*, **294**, 28–42, https://doi.org/10.1016/J.GCA.2020.11.018.

Tucker, J.M., Hauri, E.H., Pietruszka, A.J., Garcia, M.O., Marske, J.P. and Trusdell, F.A. 2019. A high carbon content of the Hawaiian mantle from olivine-hosted melt inclusions. *Geochimica et Cosmochimica Acta*, **254**, 156–172, https://doi.org/10.1016/J.GCA.2019.04.001.

Usui, T., Alexander, C.M.O.D., Wang, J., Simon, J.I. and Jones, J.H. 2012. Origin of water and mantle–crust interactions on Mars inferred from hydrogen isotopes and volatile element abundances of olivine-hosted melt inclusions of primitive shergottites. *Earth and Planetary Science Letters*, **357**–**358**, 119–129, https://doi.org/10.1016/J.EPSL.2012.09.008.

Wadhwa, M. 2008. Redox Conditions on Small Bodies, the Moon and Mars. *Reviews in Mineralogy and Geochemistry*, **68**, 493–510, https://doi.org/10.2138/RMG.2008.68.17.

Wallace, P.J. and Carmichael, I.S.E. 1994. S speciation in submarine basaltic glasses as determined by measurements of SKa X-ray wavelength shifts. *American Mineralogist*, **79**, 161–167.

Wallace, P.J. and Edmonds, M. 2011. The Sulfur Budget in Magmas: Evidence from Melt Inclusions, Submarine Glasses, and Volcanic Gas Emissions. *Reviews in Mineralogy and Geochemistry*, **73**, 215–246, https://doi.org/10.2138/rmg.2011.73.8.

Wang, W., Kelley, K.A., et al. 2021. Volatile Element Evidence of Local MORB Mantle Heterogeneity Beneath the Southwest Indian Ridge, 48°–51°E. *Geochemistry, Geophysics, Geosystems*, **22**, e2021GC009647, https://doi.org/10.1029/2021GC009647.

Wanless, V.D., Shaw, A.M., Behn, M.D., Soule, S.A., Escartín, J. and Hamelin, C. 2015. Magmatic plumbing at Lucky Strike volcano based on olivine-hosted melt inclusion compositions. *Geochemistry, Geophysics, Geosystems*, **16**, 126–147, https://doi.org/10.1002/2014GC005517.

Wetzel, D.T., Rutherford, M.J., Jacobsen, S.D., Hauri, E.H. and Saal, A.E. 2013. Degassing of reduced carbon from planetary basalts. *Proceedings of the National Academy of Sciences*, **110**, 8010–8013, https://doi.org/10.1073/PNAS.1219266110.

Wetzel, D.T., Hauri, E.H., Saal, A.E. and Rutherford, M.J. 2015. Carbon content and degassing history of the lunar volcanic glasses. *Nature Geoscience 2015 8:10*, **8**, 755–758, https://doi.org/10.1038/ngeo2511.

Wieser, P.E., Lamadrid, H., et al. 2021. Reconstructing Magma Storage Depths for the 2018 Kīlauean Eruption From Melt Inclusion CO2 Contents: The Importance of Vapor Bubbles.

Geochemistry, Geophysics, Geosystems, **22**, e2020GC009364, https://doi.org/10.1029/2020GC009364.

Wieser, P.E., Iacovino, K., Matthews, S., Moore, G. and Allison, C.M. 2022. VESIcal: 2. A Critical Approach to Volatile Solubility Modeling Using an Open-Source Python3 Engine. *Earth and Space Science*, **9**, e2021EA001932, https://doi.org/10.1029/2021EA001932.

Wilke, M., Klimm, K. and Kohn, S.C. 2011. Spectroscopic studies on sulfur speciation in synthetic and natural glasses. *Reviews in Mineralogy and Geochemistry*, **73**, 41–78, https://doi.org/10.2138/rmg.2011.73.3.

Yip, S.T.H., Biggs, J., Edmonds, M., Liggins, P. and Shorttle, O. 2022. Contrasting Volcanic Deformation in Arc and Ocean Island Settings Due To Exsolution of Magmatic Water. *Geochemistry, Geophysics, Geosystems*, **23**, e2022GC010387, https://doi.org/10.1029/2022GC010387.

Yoshioka, T., Nakashima, D., Nakamura, T., Shcheka, S. and Keppler, H. 2019. Carbon solubility in silicate melts in equilibrium with a CO-CO2 gas phase and graphite. *Geochimica et Cosmochimica Acta*, **259**, 129–143, https://doi.org/10.1016/J.GCA.2019.06.007.

Zajacz, Z. and Tsay, A. 2019. An accurate model to predict sulfur concentration at anhydrite saturation in silicate melts. *Geochimica et Cosmochimica Acta*, **261**, 288–304, https://doi.org/10.1016/J.GCA.2019.07.007.

1165 # 7 Figure captions

1166

1167 *Figure 1* Calculated values of P^{v}_{sat} vs. $\log_{10}(f_{O2})$ for a Hawaiian tholeiitic melt at 1200 °C with
1168 H_2O-eq = 3 wt%, CO_2-eq = 1000 ppm, and S-eq = 0 ppm (cases 1 and 2, black horizontal lines
1169 and blue curves, respectively, from this study; and the horizontal black-dashed line is similar to
1170 case 1 but calculated using VolatileCalc (Newman and Lowenstern 2002)) or S-eq = 1000 ppm
1171 (case 3, yellow curve). For these conditions, none of the melt compositions are supersaturated
1172 with respect to graphite, sulfide, or anhydrite. The f_{O2} ranges for different tectonic settings from
1173 Cottrell et al. (2021) are shown by horizonal blue bars below the main figure (the extent of each
1174 bar shows the range and the black vertical line shows the mode) for mid-ocean ridge (MORB:
1175 light blue), ocean island (OIB: intermediate blue), and arc (Arc: dark blue) basalts based on
1176 XANES measurements of Fe^{3+}/Fe_T of glass. The upper limit of f_{O2} for lunar and martian magmas
1177 (L/M) is shown by a capped black horizontal arrow (Wadhwa 2008; Gaillard *et al.* 2021)

1178 *Figure 2* Calculated values of p_i's (top row), species fraction in the melt (middle row), and x^{v}_{i}'s
1179 (bottom row) vs. $\log_{10}(f_{O2})$ for cases 1–3 discussed in the text. All calculations are for a Hawaiian
1180 tholeiitic melt at 1200 °C with H_2O-eq = 3 wt%, CO_2-eq = 1000 ppm, and S-eq = 0 ppm (case 1
1181 shown in both columns and case 2 shown in column 1) or S-eq = 1000 ppm (case 3 shown in
1182 column 2). The red curves in both columns are for H-bearing species (including CH_4, but not
1183 H_2S); blue curves for C-bearing species (including OCS, but not CH_4); and yellow curves in
1184 column 2 are for S-bearing species (including H_2S, but not OCS). Results for case 1 (indicated
1185 by a superscript circle, °) are shown for reference in (**a**–**b**) and (**e**–**f**): H_2O is a dashed horizontal
1186 black line and CO_2 is a dotted horizontal black line. For melt speciation in (**c**–**d**), the blue curves
1187 show the fractions of C in different C-bearing species as a fraction total C in the melt (i.e., CO_2 =

1188 solid, CO = dash, CH_4 = dot), and these fractions sum to one. The red curves show the fractions
1189 of H in different H-bearing species as a fraction total H in the melt (H_2O_T = solid, H_2 = dash,
1190 CH_4 = dot, H_2S = dot-dash), which also sum to one. The yellow curves show the fractions of S in
1191 different S-bearing species as a fraction total S in the melt (SO_4^{2-} = solid, $*S^{2-}$ = dash, H_2S = dot-
1192 dash, $S^{2-}_T = *S^{2-} + H_2S$ = dot). For the S-bearing melt species shown in (**d**), both [$SO_4^{2-} + *S^{2-} +$
1193 H_2S] and [$SO_4^{2-} + S^{2-}_T$] equal one. For the vapor speciation in (**e**–**f**), the sum of all coloured
1194 curves is one at any given f_{O2}, and likewise for the horizontal black reference lines representing
1195 case 1. The p_i's and x^v_i's of S_2, H_2S, and OCS in (**b**,**f**) are always near zero (i.e., close to the x-
1196 axis) on this scale (see Figure 3 for a zoomed in version). For these conditions, none of the melt
1197 compositions are supersaturated with respect to graphite, sulfide, or anhydrite. The f_{O2} ranges for
1198 different settings are as described in Figure 2.

1199 *Figure 3* Variations with $\log_{10}(f_{O2})$ for a Hawaiian tholeiitic melt at 1200 °C with H_2O-eq = 3
1200 wt%, CO_2-eq = 1000 ppm, and S-eq 1000 ppm (case 3) of the partial pressures of individual S-
1201 bearing vapor species (S_2 – dash, SO_2 – solid, and H_2S – dot in yellow; OCS in blue dash), their
1202 sum (ΣS-species = $p_{S2} + p_{SO2} + p_{H2S} + p_{OCS}$ in solid black), ΔP^v_{sat} (dash black), and P^v_{sat}[case 4]
1203 ([S-O] = grey; i.e., $p_{S2} + p_{SO2} + p_{O2}$ for S-eq = 1000 ppm, CO_2-eq = 0 ppm, and H_2O-eq = 0 wt%;
1204 Hughes *et al.,* 2023). For these conditions, none of the melt compositions are supersaturated
1205 with respect to graphite, sulfide, or anhydrite. The f_{O2} ranges for different settings are as
1206 described in Figure 2.

1207 *Figure 4* Effects of varying volatile concentrations (S, H, and C) and f_{O2} on P^v_{sat} for a Hawaiian
1208 tholeiitic melt at 1200 °C. **(a)** CO_2 against H_2O dissolved in vapor-saturated melt contoured for
1209 P^v_{sat} (bars; black solid curves) calculated assuming case 1. The grey dashed lines in **(a)** are the
1210 H_2O-CO_2 concentrations shown in (**b**–**d**) and the grey star is case 1 described in Section 3.1.1.

(b–d) Contours of ΔP^{v}_{sat} (bars, difference between case 3 [C-O-H-S] and case 1 [oxidised C-O-H]): **(b)** H_2O-eq = 3 wt%, CO_2-eq = 1000 ppm, and S-eq = 0–2000 ppm; **(c)** H_2O-eq = 0–5 wt%, CO_2-eq = 1000 ppm, and S-eq = 1000 ppm; and **(d)** H_2O-eq = 3 wt%, CO_2-eq = 0–2000 ppm, and S-eq = 1000 ppm. The grey dashed lines in (**b**–**d**) correspond to case 3 described in Section 3.1.3 and illustrated in Figure 1, Figure 2b,d,f, and Figure 3 (H_2O-eq = 3 wt%, CO_2-eq = 1000, and S-eq = 1000 ppm), and the black solid curves are the trace of the maximum in P^{v}_{sat}. For these conditions, none of the melt compositions are supersaturated with respect to graphite or anhydrite, but are supersaturated with respect to sulfide above the white dotted curve. The f_{O2} ranges for different settings are as described in Figure 1.

Figure 5 The **(a)** magnitude and **(b)** position of the maximum in P^{v}_{sat} for a Hawaiian tholeiitic melt at 1200 °C using case 3 [C-O-H-S] containing: H_2O-eq = 3 wt%, CO_2-eq = 1000 ppm, and S-eq = 0–2000 ppm (yellow); H_2O-eq = 0–5 wt%, CO_2-eq = 1000 ppm, and S-eq = 1000 ppm (red); and H_2O-eq = 3 wt%, CO_2-eq = 0–2000 ppm, and S-eq = 1000 ppm (blue). The *x*-axis is the concentration of volatile species that is changing for each curve (e.g., for the yellow curves it is S-eq). Although rotated, the curves in **(b)** are the same as the black curves in Figure 4b–d.

Figure 6 Melt inclusion (mi, circles) and matrix glass (mg, diamonds) data for natural terrestrial samples from the literature, for which H_2O-eq, CO_2-eq, and S-eq and Fe^{3+}/Fe_T have been measured. **(a–c)** Mid Ocean Ridge Basalts (MORB): American-Antarctic Ridge = grey, Kolbeinsey Ridge = black, Mid-Atlantic Ridge = blue, Reykjanes Ridge = red, and South-West Indian Ridge = yellow; **(d–f)** Ocean Island Basalts (OIB): Hawai'i = yellow, and Iceland = red; and **(g–i)** arc basalts: Bonin = blue, and Marianas = grey. **(a,d,g)** Measured CO_2-eq vs. H_2O-eq, with calculated isobars (in kbar) using case 1; and **(b,e,h)** measured S-eq vs. calculated f_{O2} from measured Fe^{3+}/Fe_T, with an indication of the location of the sulfur solubility minimum using case

4 [S-O, 1000 ppm S-eq] in grey – it does not use the *y*-axis values and is there to show the f_{O2}-position of the SS^{min}. **(c,f,i)** ΔP^{v}_{sat} vs. P^{v}_{sat} (using case 1: only oxidised C-O-H species), where ΔP^{v}_{sat} is the difference between case 3 (all C-O-H-S species; calculated using measured volatile contents and melt composition at 1200 °C) and case 1. The grey solid lines show relative % errors (i.e., $100*[\Delta P^{v}_{sat}/P^{v}_{sat}]$) as labelled on the line. None of the melt compositions are supersaturated with respect to graphite, sulfide, or anhydrite. MORB matrix glasses are from American-Antarctic Ridge (Le Voyer *et al.* 2019), Kolbeinsey Ridge (Le Voyer *et al.* 2019), Mid-Atlantic Ridge (Le Voyer *et al.* 2019), Reykjanes Ridge (Nichols *et al.* 2002; Shorttle *et al.* 2015), and South-West Indian Ridge (Wang *et al.* 2021). Hawai'i melt inclusions are from Kīlauea (Moussallam *et al.* 2016) and matrix glasses are from Mauna Kea (Brounce *et al.* 2017). Iceland melt inclusions are from 1783–84 Laki eruption (Hartley *et al.* 2015, 2017). Marianas melt inclusions are from Agrigan, Sarigan, and Alamagan volcanoes (Kelley and Cottrell 2012; Brounce *et al.* 2014) and matrix glasses are from the Mariana Trough and Fina Nagu (Brounce *et al.* 2014, 2016). Bonin matrix glasses are forearc basalts (Brounce *et al.* 2021; Coulthard Jr *et al.* 2022).

Figure 7 Melt inclusion (mi, circles) and matrix glass (mg, diamonds) data for natural lunar (blue; Saal and Hauri 2021) and martian (red; Usui *et al.* 2012) samples from the literature, where H_2O-eq, CO_2-eq, and S-eq have been measured. Measured H_2O-eq against **(a)** CO_2-eq and **(b)** S-eq. ΔP^{v}_{sat} (difference between cases 3 and 1) calculated for each measured glass composition at 1200 °C against **(c–d)** $\log[f_{O2}]$ and **(e–f)** P^{v}_{sat} (case 1), where for the solid region of each curve the melt is not supersaturated with respect to graphite, sulfide, or anhydrite (labelled "stable") but the dashed regions indicate the melt is supersaturated with respect to sulfide and/or graphite (labelled "metastable"; for these conditions the melt is never

1257 supersaturated with respect to anhydrite). The extent of each vertical line in **(e–f)** corresponds to
1258 the vertical range of a single curve in **(c–d)**. Lunar samples are shown in **(c,e)** and martian
1259 samples in **(d,f)**. In **(e–f)** the grey solid lines show relative % errors as labelled on the line (see
1260 Figure 6).

1261

1262

This is the peer-reviewed, final accepted version for American Mineralogist, published by the Mineralogical Society of America.
The published version is subject to change. Cite as Authors (Year) Title. American Mineralogist, in press.
DOI: https://doi.org/10.2138/am-2022-8739. http://www.minsocam.org/

8 Tables

Table 1 Homogeneous vapor equilibria considered in our model.

Reaction	Equilibrium constant	Eq no.
$H_2 + 0.5O_2 \rightleftarrows H_2O$	$K_{\mathrm{H}} = \frac{f_{\mathrm{H_2O}}}{f_{\mathrm{H_2}} f_{\mathrm{O_2}}^{0.5}}$	(5)
$CO + 0.5O_2 \rightleftarrows CO_2$	$K_{\mathrm{C}} = \frac{f_{\mathrm{CO_2}}}{f_{\mathrm{CO}} f_{\mathrm{O_2}}^{0.5}}$	(6)
$0.5S_2 + O_2 \rightleftarrows SO_2$	$K_{\mathrm{S}} = \frac{f_{\mathrm{SO_2}}}{f_{\mathrm{S_2}}^{0.5} f_{\mathrm{O_2}}}$	(7)
$CH_4 + 2O_2 \rightleftarrows CO_2 + 2H_2O$	$K_{\mathrm{CH}} = \frac{f_{\mathrm{CO_2}} f_{\mathrm{H_2O}}^2}{f_{\mathrm{CH_4}} f_{\mathrm{O_2}}^2}$	(8)
$0.5S_2 + H_2O \rightleftarrows H_2S + 0.5O_2$	$K_{\mathrm{HS}} = \frac{f_{\mathrm{H_2S}} f_{\mathrm{O_2}}^{0.5}}{f_{\mathrm{S_2}}^{0.5} f_{\mathrm{H_2O}}}$	(9)
$2CO_2 + OCS \rightleftarrows 3CO + SO_2$	$K_{\mathrm{SC}} = \frac{f_{\mathrm{CO}}^3 f_{\mathrm{SO_2}}}{f_{\mathrm{CO_2}}^2 f_{\mathrm{OCS}}}$	(10)

Notes: $K_{\mathrm{X(Y)}}$ are equilibrium constants, which depend on T but are independent of P and are given in Supplementary Material Section 3.1; and f_i is the fugacity of species i.

Table 2 Solubility mechanisms and functions considered in our model.

Solubility mechanism	Solubility function	Eq no.
$H_2(v) \rightleftarrows H_{2,\mathrm{mol}}(m)$	$f_{\mathrm{H_2}} = \frac{w^m_{\mathrm{H_{2,mol}}}}{C_{\mathrm{H_{2,mol}}}}$	(11)
$H_2O(v) \rightleftarrows H_2O_{\mathrm{mol}}(m)$ $H_2O(m) + O^{2-}(m) \rightleftarrows 2OH^-(m)$	$f_{\mathrm{H_2O}} \approx \frac{\left(x^m_{\mathrm{H_2O_T}}\right)^2}{C_{\mathrm{H_2O_T}}}$	(12)

This is the peer-reviewed, final accepted version for American Mineralogist, published by the Mineralogical Society of America.
The published version is subject to change. Cite as Authors (Year) Title. American Mineralogist, in press.
DOI: https://doi.org/10.2138/am-2022-8739. http://www.minsocam.org/

$CO(v) \rightleftarrows CO_{mol}(m)$	$f_{CO} = \frac{w^m_{CO_{mol}}}{C_{CO_{mol}}}$	(13)
$CO_2(v) + O^{2-}(m) \rightleftarrows CO_3^{2-}(m)$	$f_{CO_2} = \frac{x^m_{CO_3^{2-}}}{C_{CO_3^{2-}}}$	(14)
$CH_4(v) \rightleftarrows CH_{4,mol}(m)$	$f_{CH_4} = \frac{w^m_{CH_{4,mol}}}{C_{CH_{4,mol}}}$	(15)
$0.5S_2(v) + O^{2-}(m) \rightleftarrows {}^*S^{2-}(m) + 0.5O_2(v)$	$f_{S_2} = \left(\frac{w^m_{{}^*S^{2-}}}{C_{{}^*S^{2-}}}\right)^2 f_{O_2}$	(16)
$0.5S_2(v) + 1.5O_2(v) + O^{2-}(m) \rightleftarrows SO_4^{2-}(m)$	$f_{S_2} = \left(\frac{w^m_{SO_4^{2-}}}{C_{SO_4^{2-}}}\right)^2 f_{O_2}^{-3}$	(17)
$H_2S(v) \rightleftarrows H_2S_{mol}(m)$	$f_{H_2S} = \frac{w^m_{H_2S_{mol}}}{C_{H_2S_{mol}}}$	(18)

Notes: v = vapor; m = melt; mol = molecular; f_i = fugacity of species i; x^m_i = mole fraction or w^m_i = concentration (depending on the units) of species i in the melt; C_i = solubility of species i, which is the constant of proportionality between the fugacity(ies) and the mole fraction/concentration of species i in the melt; ${}^*S^{2-}$ = sulfide associated with cations in the silicate melt, rather than associated with H, i.e., H_2S_{mol}. Details of solubilities are given in Supplementary Material Section 3.2.

This is the peer-reviewed, final accepted version for American Mineralogist, published by the Mineralogical Society of America.
The published version is subject to change. Cite as Authors (Year) Title. American Mineralogist, in press.
DOI: https://doi.org/10.2138/am-2022-8739. http://www.minsocam.org/

9 Figures

Figure 1

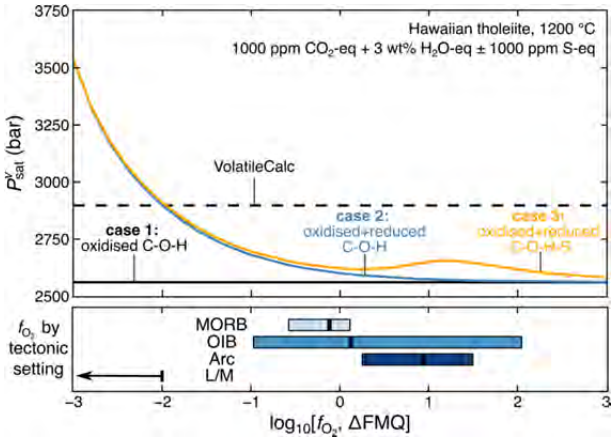

This is the peer-reviewed, final accepted version for American Mineralogist, published by the Mineralogical Society of America.
The published version is subject to change. Cite as Authors (Year) Title. American Mineralogist, in press.
DOI: https://doi.org/10.2138/am-2022-8739. http://www.minsocam.org/

Figure 2

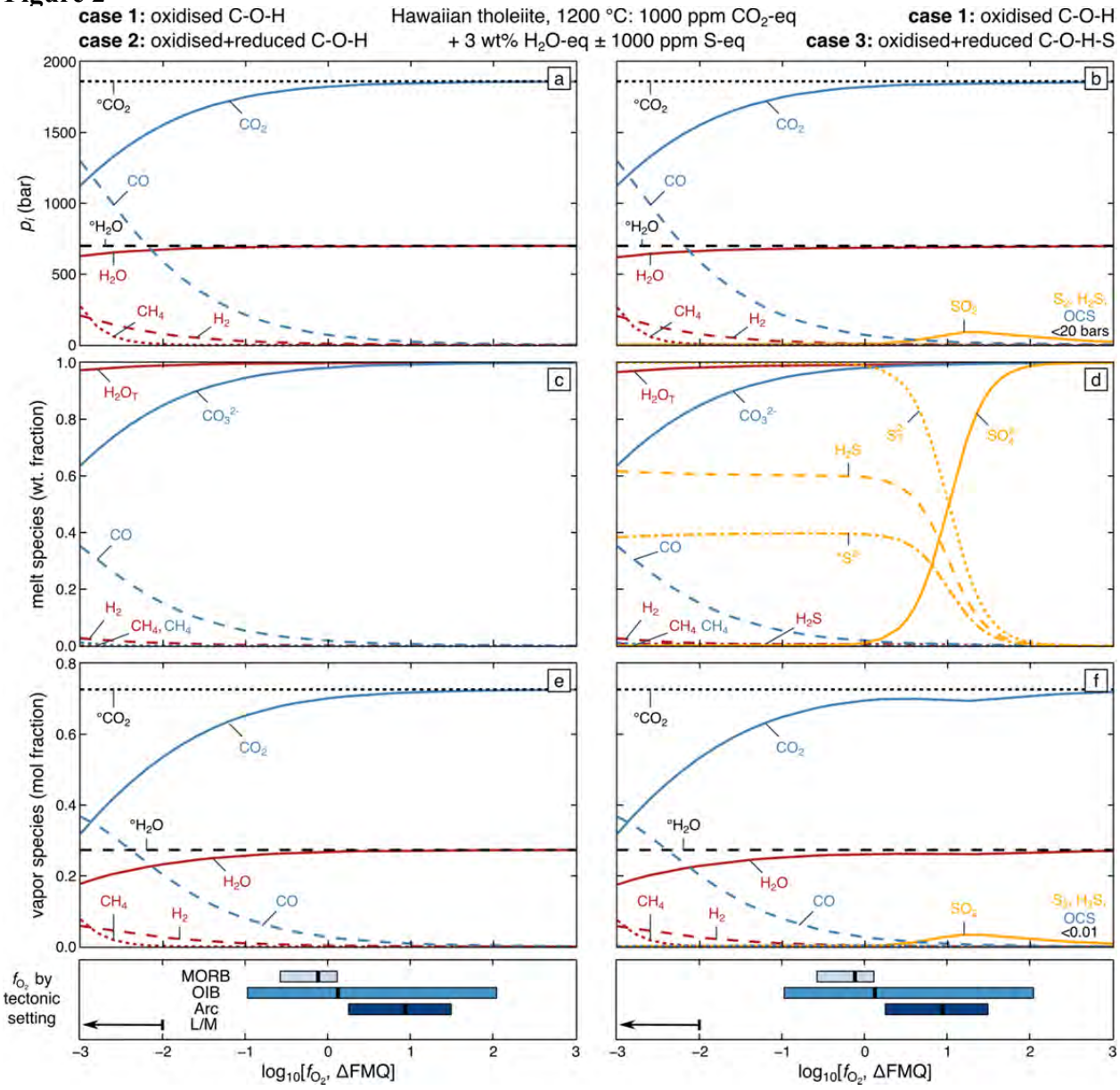

This is the peer-reviewed, final accepted version for American Mineralogist, published by the Mineralogical Society of America.
The published version is subject to change. Cite as Authors (Year) Title. American Mineralogist, in press.
DOI: https://doi.org/10.2138/am-2022-8739. http://www.minsocam.org/

1287 **Figure 3**

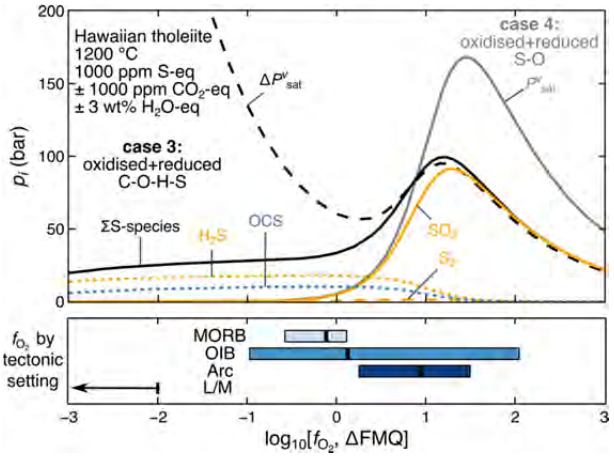

1288

1289

This is the peer-reviewed, final accepted version for American Mineralogist, published by the Mineralogical Society of America.
The published version is subject to change. Cite as Authors (Year) Title. American Mineralogist, in press.
DOI: https://doi.org/10.2138/am-2022-8739. http://www.minsocam.org/

Figure 4

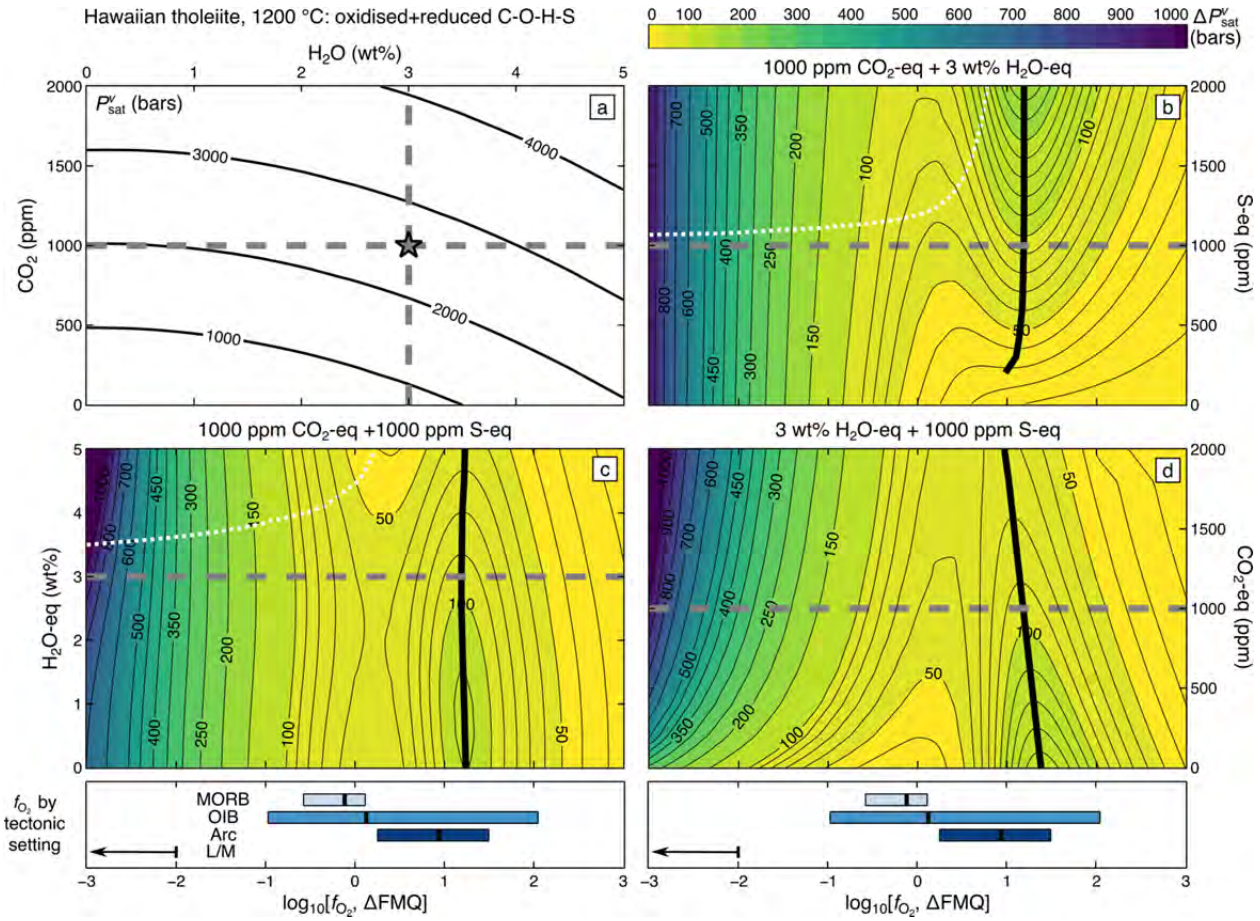

1291

1292

1293

This is the peer-reviewed, final accepted version for American Mineralogist, published by the Mineralogical Society of America.
The published version is subject to change. Cite as Authors (Year) Title. American Mineralogist, in press.
DOI: https://doi.org/10.2138/am-2022-8739. http://www.minsocam.org/

1294 **Figure 5**

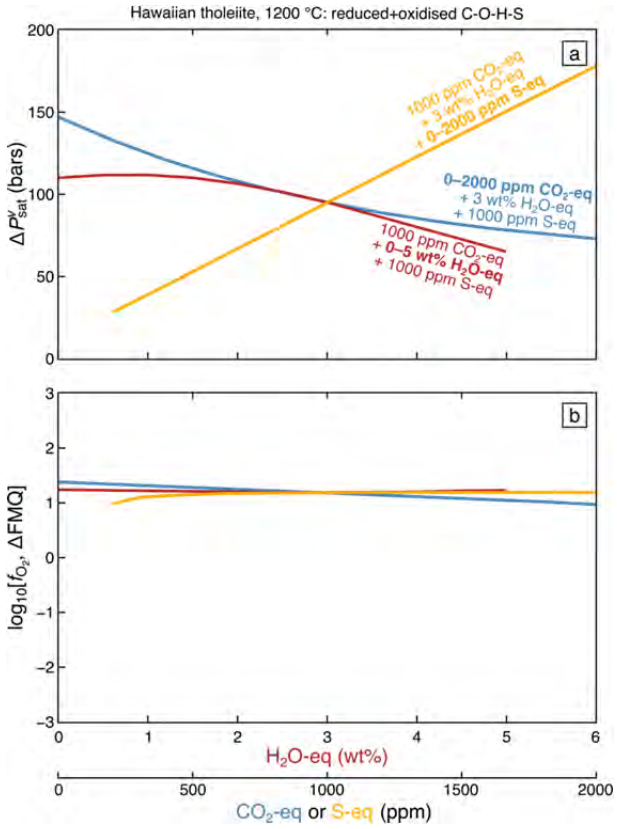

1295

1296

This is the peer-reviewed, final accepted version for American Mineralogist, published by the Mineralogical Society of America.
The published version is subject to change. Cite as Authors (Year) Title. American Mineralogist, in press.
DOI: https://doi.org/10.2138/am-2022-8739. http://www.minsocam.org/

1297 **Figure 6**

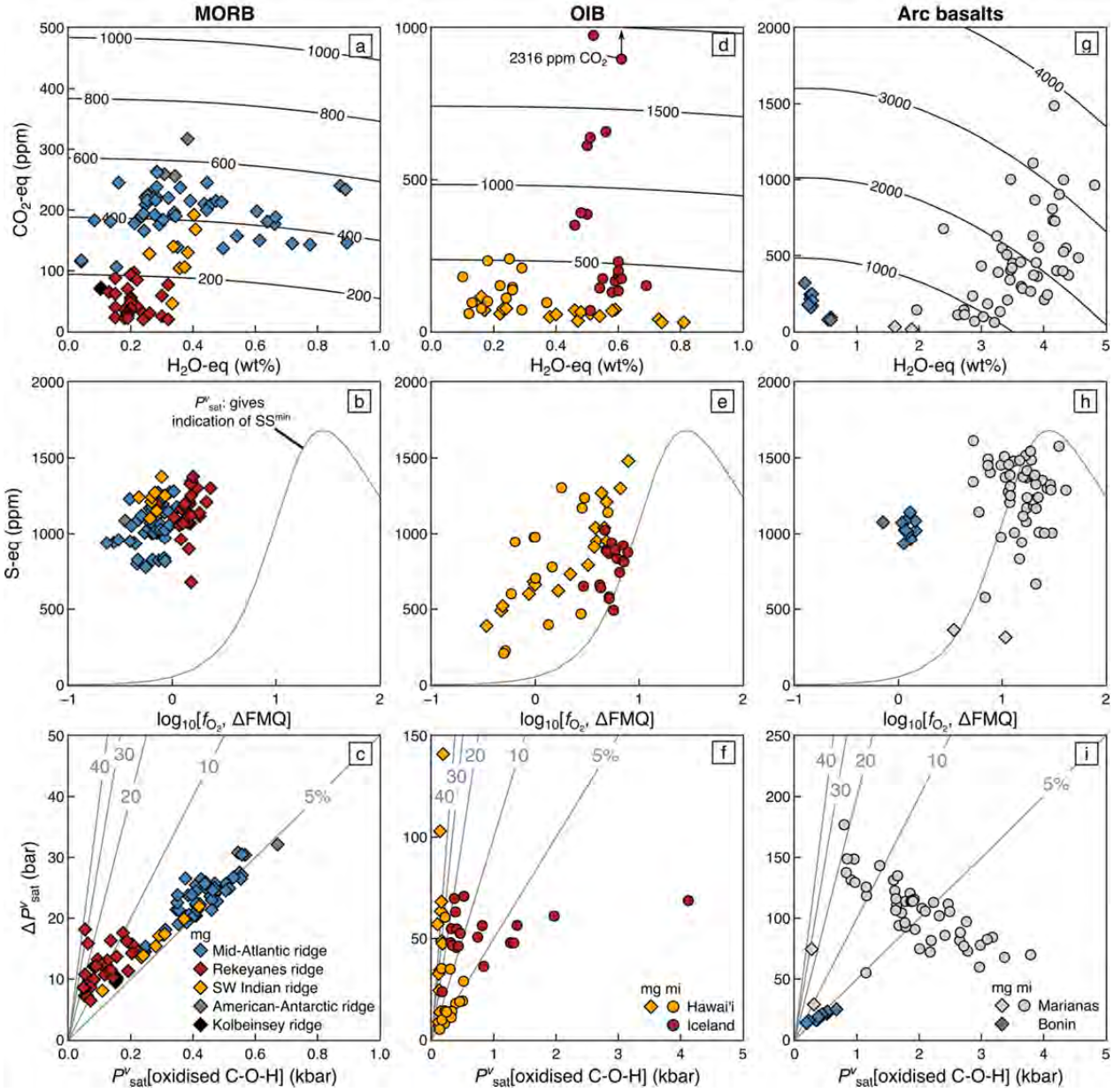

1298

1299

This is the peer-reviewed, final accepted version for American Mineralogist, published by the Mineralogical Society of America.
The published version is subject to change. Cite as Authors (Year) Title. American Mineralogist, in press.
DOI: https://doi.org/10.2138/am-2022-8739. http://www.minsocam.org/

Figure 7